Hydrodynamic properties of a flexible pipe in bidirectionally sheared flows undergoing vortex-induced vibration

Xuepeng Fu [1], Shixiao Fu[1]† , Chang Liu[2], Jiawei Shen[1,3] and Zhibo Niu[1]

[1]State Key Laboratory of Ocean Engineering, Shanghai Jiao Tong University, Shanghai 200240, China

[2]School of Mechanical, Aerospace, and Manufacturing Engineering, University of Connecticut, Storrs, CT 06269, USA

[3]Department of Marine Technology, Norwegian University of Science and Technology, Trondheim 7491, Norway

(Received xx; revised xx; accepted xx)

The hydrodynamics of vortex-induced vibration of a flexible pipe in bidirectionally sheared flows are investigated through combined experimental and numerical approaches. Such bidirectionally sheared flows are inspired by subsurface currents induced by internal solitons widely occurring in the ocean, which feature oppositely directed flow velocities along the flexible pipe. Experiments are conducted in an ocean basin using a tensioned pipe with distributed strain sensors, and numerical simulations are conducted by a validated strip method based framework. The mean in-line displacement, mean drag, shear force, and bending moment are characterized. The mean in-line displacement, maximized over the spanwise direction, exhibits an approximately quadratic dependence on the maximum velocity in bidirectionally sheared flow. In contrast, the mean drag coefficient remains nearly unchanged with increasing flow velocity. Both trends are cross-validated via experiments and simulations. Furthermore, empirical expressions are proposed to describe the influence of background flow velocities on the shear force and bending moment. Excitation and added mass coefficients associated with dominant frequency response and time-varying hydrodynamic coefficients considering multi-frequency responses are extracted and analyzed. The results show that the phase difference between the cross-flow and in-line responses retains an antisymmetric distribution, whereas the excitation coefficients exhibit quasi-symmetric patterns around the mid-span. The time-dependent added-mass coefficient is strongly correlated with the wake pattern, with negative values occurring predominantly during P+S and 2P vortex shedding patterns. Moreover, spectral proper orthogonal decomposition is employed to link the dominant VIV frequencies of the flexible pipe with the surrounding flow field. The results indicate a clear transition in which the dominant flow-field frequency follows the Strouhal frequency at lower velocity, but aligns with the structural vibration frequency at higher velocity associated with the occurrence of the lock-in phenomenon.

Key words: Flow-structure interactions, vortex dynamics, vortex shedding

† Email address for correspondence: shixiao.fu@sjtu.edu.cn

1. Introduction

Vortex-induced vibration (VIV) of long flexible structures has been the subject of extensive research in ocean engineering applications such as marine risers and umbilical cables (Bearman 1984; Resvanis & Vandiver 2022; Huera-Huarte 2025), in civil engineering applications such as large-span bridges (Ge *et al.* 2022), and more recently in renewable energy structures including wind turbine blades (Grinderslev *et al.* 2022; Fu *et al.* 2026) and towers (Livanos 2018).

Flexible pipes present significant challenges for the direct measurement of vortex-induced hydrodynamic force distributions along their length due to continuous deformation and spatially distributed dynamic responses. In contrast, both motion and hydrodynamic force measurements are relatively straightforward for rigid cylinders. As a result, the canonical model for studying the vortex-induced vibration of flexible structures is a circular rigid cylinder placed in a uniform flow (Tian *et al.* 2023), allowed to vibrate freely in both the cross-flow (CF) and in-line (IL) directions (Bearman 1984; Williamson & Govardhan 2004; Fu *et al.* 2025*a*; Han *et al.* 2023; Cheng *et al.* 2024; Benner *et al.* 2025). Key response characteristics such as the vibration amplitude and frequency have been extensively investigated, including phenomena such as lock-in (Gabbai & Benaroya 2005; Williamson & Govardhan 2008), the critical mass ratio (Govardhan & Williamson 2000), and the Griffin plot (Govardhan & Williamson 2006).

Numerous methods have been proposed to present VIV hydrodynamic forces of the bluff cylinder, among which the approaches developed by Sarpkaya (1995) and Thorsen *et al.* (2017) remain widely adopted. Sarpkaya (1995, 2004) proposed a VIV force decomposition method consisting of one component in phase with velocity, representing the energy exchange between the fluid and the structure, and another component in phase with acceleration, representing the added mass effect. Thorsen *et al.* (2017) improved this decomposition by introducing a consistent drag force model that connects the forces in the IL and CF directions. Due to the difficulty of fully exploring the parameter space in traditional freely vibrating experiments, forced vibration tests with prescribed harmonic motion (Gopalkrishnan 1993; Aronsen & Larsen 2007; Patel *et al.* 2023) have been conducted to investigate the hydrodynamic characteristics of rigid cylinders undergoing VIV. Comprehensive experiments including CF-only forced motion (Gopalkrishnan 1993), IL-only forced motion (Aronsen & Larsen 2007) and IL & CF forced motion (Yin & Larsen 2011; Dahl 2008; Dahl *et al.* 2010) are conducted to determine the VIV excitation range and excitation coefficient curve.

Slender structures in applications are subjected to a wide variety of flow conditions. VIV experiments on flexible risers under various flow conditions provide a fundamental understanding of the VIV characteristics of flexible pipes and serve as a benchmark for numerical analysis. Flexible pipes can be categorized into tension dominated (Huera-Huarte 2006; Zheng *et al.* 2014*a*; Duan *et al.* 2021) and bending stiffness dominated (Nielsen *et al.* 2002) types, depending on the relative contributions of tension and bending stiffness to their natural frequencies. Tension-dominated flexible pipe VIV is typically more complicated with multi-mode coupled responses (Zheng *et al.* 2014*b*). Numerous VIV experiments on flexible risers have been conducted under various flow conditions: uniform flow (Chaplin *et al.* 2005), linearly sheared flow (Tognarelli *et al.* 2004; Trim *et al.* 2005), three-dimensional flow (Kim *et al.* 2022), and lake tests (Vandiver *et al.* 2005).

Due to the challenges associated with the direct measurement of VIV hydrodynamic force distributions of the flexible pipe, recent research has focused on estimating these force distributions indirectly through strain or displacement measurements (Wu 2011; Song *et al.* 2016*a*). For mono-frequency VIV responses, the hydrodynamic behavior can be accurately characterized using constant excitation and added mass coefficients (Bourguet *et al.* 2012).

Huera-Huarte *et al.* (2006) were among the first to employ inverse finite element analysis to estimate the hydrodynamic force distribution in a stepped-flow VIV experiment. Song *et al.* (2016*a*) proposed a hydrodynamic force estimation method based on inverse finite element method in which the hydrodynamic forces were directly estimated using the differential governing equations of a tensioned beam model, and applied for several flexible riser experiments under different flow conditions at Shanghai Jiao Tong University. In addition to the least squares method, Wu (2011) developed a hydrodynamic coefficient identification approach using Kalman filtering and an optimization-based approach, based on experimental data obtained from tests conducted at the Norwegian Marine Technology Research Institute. These methods have been applied for the mono-frequency VIV under uniform flow and linearly sheared flow analysis. However, these studies, which are based on the assumption of constant hydrodynamic coefficients, become inadequate when addressing multi-frequency or modulated VIV responses, where the hydrodynamic forces exhibit strong nonlinearity. To capture the unsteady hydrodynamic behavior under such conditions, time-varying hydrodynamic coefficients have been introduced (Liu *et al.* 2018, 2020; Fu *et al.* 2022*b*), which can accurately capture the hydrodynamics of multi-frequency VIV under shear flow (Liu *et al.* 2018), and modulated VIV under time-varying oscillatory flow (Liu *et al.* 2020; Fu *et al.* 2022*b*). This approach provides a robust framework to demonstrate the time-varying characteristics of multi-frequency and modulated VIV hydrodynamics.

Computational fluid dynamics approaches are mainly adopted to investigate the fluid characteristics and fluid-structure interaction behavior of flexible pipes. For low aspect ratio flexible pipe and bluff cylinder VIV experiments, flow field measurement techniques can be employed to capture the fluid domain (Govardhan & Williamson 2000; Jung *et al.* 2018). However, accurately measuring flow characteristics remains challenging, particularly for high aspect ratio flexible pipes VIV. Numerical studies focusing on flexible pipes remain relatively limited due to the complex fluid-structure interactions involving multiple vibration modes and nonlinear wake dynamics. Some simulation results of uniform flow (Evangelinos & Karniadakis 1999; Willden & Graham 2001; Dahl *et al.* 2007; Modarres-Sadeghi *et al.* 2010; Bourguet *et al.* 2011*b*, 2012; Fan *et al.* 2019*b*; Wang *et al.* 2021*b*), and linearly sheared flow (Bourguet *et al.* 2011*a*, 2012, 2013) have established fundamental knowledge for flexible pipe VIV. Newman & Karniadakis (1997) applied direct numerical simulation (DNS) of a 4π long flexible pipe at Reynolds numbers of approximately 100, revealing the fundamental VIV characteristics such as traveling wave wake patterns. Furthermore, Evangelinos & Karniadakis (1999) and Bourguet *et al.* (2011*a*) conducted DNS simulation to investigate the fundamental characteristics of flexible pipe at Reynolds numbers of approximately 1000 using Nektar++. Willden & Graham (2004) applied the velocity-vorticity method to simulate flexible pipe VIV at Reynolds numbers around 300 and named VIVIC. Fan *et al.* (2019*b*) and Wang *et al.* (2021*b*) applied strip methods to numerically investigate flexible pipe VIV at relatively high Reynolds numbers of approximately 2000 using Nektar++, illustrating the relationships between flexible pipe free vibration and the forced vibration of a bluff cylinder. In the strip method, the flow is treated as a series of two-dimensional sections coupled with a three-dimensional beam model, and few studies have been conducted to improve the method (Bao *et al.* 2016; Deng *et al.* 2020).

For the numerical simulation of vortex-induced vibration of long flexible pipes, the strip method offers a more practical and feasible approach. Recent studies have attempted to connect wake dynamics with hydrodynamic coefficients via simultaneous flow visualization and structural response measurements. Bourguet *et al.* (2011*b*) proposed that the excitation coefficient is related to the vibration phase difference. Fan *et al.* (2019*b*) and Wang *et al.* (2021*a*) reported that vortex shedding patterns such as 2S (two single vortices), 2P (two pairs of vortices), or P+S (one pair plus one single vortex) are related to the added mass

coefficients; a negative added mass coefficient is associated with the P+S and 2P wake patterns. For wake field analysis, spectral proper orthogonal decomposition (SPOD) can be used to extract coherent flow structures in both space and time (Sieber *et al.* 2016; Towne *et al.* 2018). This ability to identify frequency-dependent flow modes makes SPOD a suitable tool for cylinder wake field analysis. SPOD has been applied to bluff body wakes (Willert 2025; Maleki *et al.* 2026) and to the wakes of VIV bluff cylinders undergoing VIV (O'Neill *et al.* 2021) and forced motion (Zhou & Zheng 2023).

A unique subsurface flow environment induced by internal waves has been observed in the South China Sea. A six-month field survey conducted in the Liuhua area by the China National Offshore Oil Corporation Research Institute (Xie *et al.* 2018) revealed a distinctive shear flow structure characterized by nearly opposite flow directions, asymmetric velocity magnitudes, and a sharp velocity gradient centered around a depth of approximately 185 meters. This bidirectionally sheared flow condition was found to occur frequently, resulting in an average exposure of approximately 18.6 hours per month. Besides the South China Sea, similar bidirectionally sheared flow has also been reported in association with internal wave in other ocean regions (Garrett & Munk 1979; MacKinnon 2017), including areas of engineering interest such as the Gulf Stream and continental slope regions. Moreover, such unique flow conditions have been observed beneath ice-covered areas in polar regions, where melting processes contribute to the formation of bidirectionally sheared flow profiles (Jacobs *et al.* 2011; Minowa *et al.* 2021).

A Joint Industry Project (JIP), Flow-Induced Forces and Their Effects on Risers and Subsea Structures (FIFERS), has been proposed and established to develop VIV prediction models for complex flow fields, including bidirectionally sheared flow. As a core component of this JIP, Fu *et al.* (2022*a*,*c*) first conducted an ocean basin experiment with a flexible pipe under bidirectionally sheared flow, observing multi-frequency responses and distinctive traveling wave patterns. Moreover, Fu *et al.* (2025*b*) developed an open-source code based on the strip method and simulated the vortex-induced vibration of a flexible pipe under bidirectionally sheared flow, with validation against experimental results. This study primarily focused on comparing the displacement responses of the flexible pipe under different flow conditions including uniform, linearly sheared and bidirectionally sheared flow cases, whereas detailed analyses of the corresponding hydrodynamic forces were not conducted.

In this paper, we further investigate the hydrodynamic properties of a flexible pipe subjected to bidirectionally sheared flow. Both experimental and numerical analyses are conducted. The experimental investigation is based on a previously published test apparatus (Fu *et al.* 2022*a*), and the numerical analysis is performed using a validated simulation framework (Fu *et al.* 2025*b*). The model has a diameter of 28.41 mm and a length of 269 diameters. This study aims to investigate the similarities and differences in hydrodynamic coefficients between bidirectionally sheared flow and unidirectional flows. Based on the experimental and numerical simulation results of VIV under bidirectionally sheared flow, four aspects of the VIV hydrodynamic characteristics are investigated: (1) how bidirectionally sheared flow modifies the mean displacement and drag coefficient distributions and the corresponding mean hydrodynamic force; (2) whether the antisymmetric velocity distribution of the bidirectionally sheared flow affects the phase distribution of the VIV response; (3) whether the excitation coefficients exhibit symmetry at the flow velocity reversal point; and (4) the relationship between the added mass coefficient and the wake vortex patterns.

This manuscript is organized as follows. Section 2 presents the experimental apparatus and setup, and the numerical method. Section 3 discusses the in-line mean drag characteristics, including the mean drag coefficient, shear force and moment, and the influence of the flow velocity distribution. Section 4 presents the hydrodynamic properties of the flexible pipe under bidirectionally sheared flow, including the dominant frequencies, time-varying

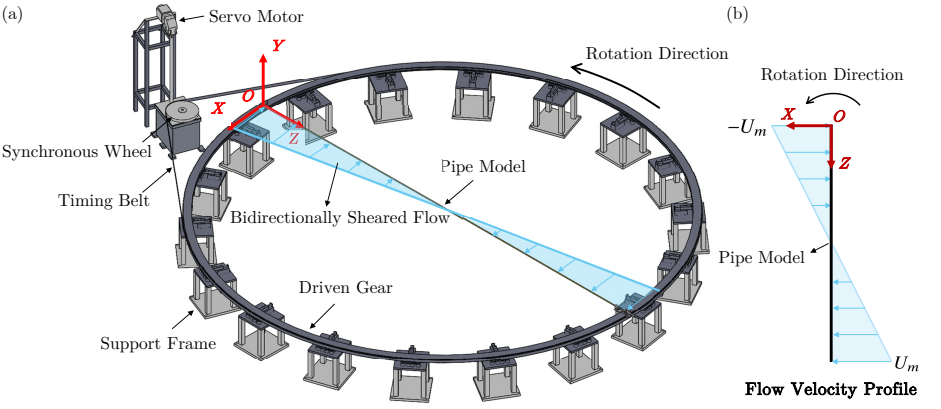

Figure 1: Diagram of the experimental set-up: (a) Diagram of the experimental apparatus. The flow field is generated by rotation of the driven gear with a bidirectionally sheared distribution. (b) The flow velocity profile from the experiment shows that the minimum negative velocity $-U_m$ occurs at $Z/L = 0$ and the maximum velocity U_m occurs at $Z/L = 1$.

hydrodynamic behavior, and corresponding wake pattern. Finally, section 5 summarizes the main conclusions of this study.

2. Experimental and numerical methods

2.1. *Experimental setup*

The experiment was conducted in an ocean basin at Shanghai Jiao Tong University. The pipe model was fixed at both ends to a circular driven gear under a pretension of 980 N. The flow field was generated by rotating the driven gear via a timing belt powered by a servo motor to generate the inflow conditions, as figure 1 shows. This novel VIV experimental apparatus has been validated through a comprehensive credibility assessment, including analyses of wake effects, vibration duration, mechanical noise, repeatability, and water-depth sensitivity, as reported in our previous work (Fu *et al.* 2022*a*) and summarized in appendix A.

The coordinate system is defined as *O*-*XYZ*, as shown in figures 1 and 2. The origin (O) is set at one end of the pipe model connected with a fixing device with no tensioner. The X, Y, and Z axes correspond to the in-line, cross-flow, and spanwise directions of the test pipe model, respectively, with the coordinate system rotating together with the pipe during the test. The rotation direction during the experiment is always along the X axis, and the effective current profile is shown with colors and arrows in figure 1.

The overview in figure 2(a) highlights the rotation system driven by a servo motor through a timing belt and synchronous wheel, with the flexible pipe model supported along the circular frame and instrumented by the data acquisition system. The rotation direction and the global coordinate system are also indicated in figure 2(a). Furthermore, figures 2(b) and (c) provide close-up views of the end-connection assemblies, including the universal joint and clamps that accommodate rotational motion while constraining the pipe, and the tensioner used at the maximum z end to maintain the prescribed axial tension and boundary condition. During the experimental test, universal joints were used to implement a pin-pin end condition for the test pipe, and due to the extra tensioner length difference, the velocity at the maximum spanwise location is approximately 4.5% lower than that at the coordinate origin. During each test, the pipe is rotated through one full cycle, which contains nearly 50 fully developed VIV periods, and further details are provided in appendix A.

The pipe model consists of an external polypropylene random copolymer pipe and an

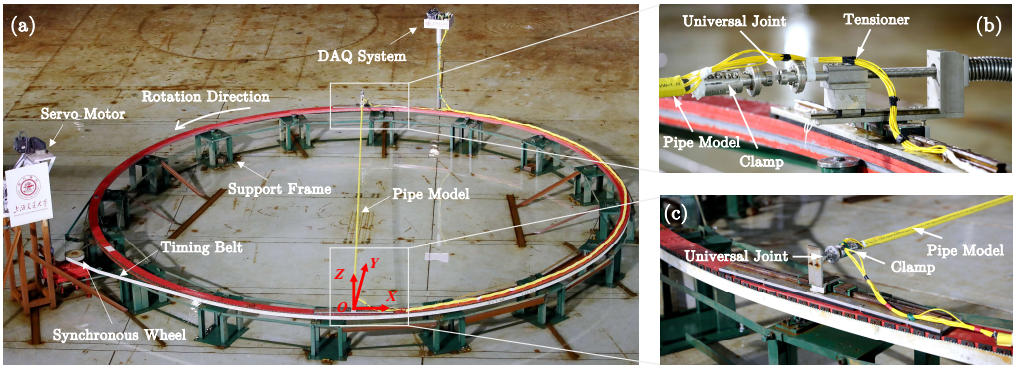

Figure 2: Experimental setup of the rotating apparatus in the ocean basin testing in air: (a) Overview of the facility. (b) Close-up of the maximum Z end connection showing the universal joint, clamp, and tensioner. (c) Close-up of the original end connection showing the universal joint and clamp.

internal copper cable. Silicone rubber is applied between the layers to prevent relative sliding. A total of 46 Fiber Bragg Grating (FBG) strain sensors, divided into four groups, are installed along the test pipe to measure dynamic strains in both the IL and CF directions, providing 14 measurement points in the IL direction and 9 measurement points in the CF direction. The LUNA SM130 optical sensing interrogator was used to measure the dynamic strain, with calibration performed prior to the tests. Modal analysis is applied to obtain the VIV displacement, while the details and strain sensor distribution are displayed in appendix B.

The physical parameters are shown in table 1. The first natural frequency in water is calculated as follows:

$$f_{c1} = \frac{\pi}{2}\sqrt{\left(1 + \frac{L^2 T_p}{\pi^2 EI}\right)\frac{EI}{\bar{m}' L^4}}, \quad \bar{m}' = \bar{m} + \frac{1}{4} C_m \rho \pi D^2, \tag{2.1}$$

where C_m is chosen as 1.00 for the free decay test (Khalak & Williamson 1997), $\rho = 998\,\mathrm{kg/m^3}$ is the density of water in the ocean basin, and $\bar{m}$ is mass per meter in air with value in table 1. The tested natural frequency is obtained by a free decay test, which differs by 5% from the theoretical value.

The relative Reynolds number $Re_r := UD/\nu$ is the Reynolds number Re with respect to the relative flow direction in the spanwise direction, and $Re_m := U_m D/\nu$ is defined as the maximum of relative Reynolds number Re_r, where U_m is the maximum velocity shown in figure 1 and where $\nu = 1 \times 10^{-6}\,\mathrm{m^2/s}$ is the kinematic viscosity of water. The apparatus is driven by a servo motor at a prescribed constant rotational speed to generate the desired flow field. A total of 58 experimental cases are conducted, maximum flow velocity U_m varied from 0.30 to 1.39 m/s with maximum Reynolds numbers Re_m ranging from 8523 to 39 490 within subcritical Re range (Achenbach 1971).

2.2. *Numerical method*

The numerical method is developed based on incompressible flow solver OpenFOAM with strip method expansion. The governing equation of the test pipe follows the tensioned Euler-Bernoulli beam model:

$$EI\frac{\partial^4 \boldsymbol{\xi}(z,t)}{\partial z^4} - \frac{\partial}{\partial z}\left[T\frac{\partial \boldsymbol{\xi}(z,t)}{\partial z}\right] + c\frac{\partial \boldsymbol{\xi}(z,t)}{\partial t} + \bar{m}\frac{\partial^2 \boldsymbol{\xi}(z,t)}{\partial t^2} = \boldsymbol{F}(z,t), \tag{2.2}$$

Parameter	Value
Pipe model length L	7.64 m
Hydrodynamic diameter D	28.41 mm
Bending stiffness EI	58.6 Nm^2
Mass per meter in air $\bar{m}$	1.24 kg/m
Mass ratio m^*	1.96
Damping ratio ζ	2.58%
Pre-tension T_p	980 N
Calculated first natural frequency f_{c1}	1.51 Hz
Calculated second natural frequency f_{c2}	3.00 Hz
Tested first natural frequency f_1	1.59 Hz

Table 1: Values of physical properties of the test pipe model.

where $\boldsymbol{\xi} = [\xi_x, \xi_y]$ is the vibration displacement in the IL and CF directions, $c = 2\bar{m}\omega_d\zeta$ is the structural damping, ω_d is the dominant frequency, T is the tension of the pipe, and $\boldsymbol{F} = [F_x, F_y]$ is the force in the IL and CF directions. In the numerical configuration, the pipe is fixed in space and is exposed to a prescribed bidirectionally sheared flow profile that is steady in time but varies along the span. Specifically, the local inflow velocity is imposed as a function of the spanwise coordinate, such that both its magnitude and direction change with Z to reproduce the equivalent bidirectionally sheared flow profile, as shown in figure 1(b). The simulations aim to avoid the wake effects of the rotating pipe and the difficulty of using a dynamic mesh. For each flow case, the simulation is advanced for approximately 60 s of physical time to ensure that the VIV response fully develops. The initial transient stage is discarded, and only the last 40% of the time record, containing at least 20 vibration periods after the response reaches a statistically steady state, is used for post-processing. A representative VIV development process is shown in appendix A, and VIV response takes about 15 s to reach the fully developed regime.

The force of each strip is obtained using incompressible Navier–Stokes equations solver OpenFOAM. Each strip domain has a size of $20D \times 50D$, with the cylinder located in the center of the domain. The boundary conditions are set as symmetry on the top and bottom boundaries, and inlet and outlet on the left and right boundaries, respectively, which is consistent with Bourguet *et al.* (2013) and Fan *et al.* (2019*b*). The flow is solved using the SST $k-\omega$ turbulence model with second-order accuracy in both spatial and temporal discretizations, and the time step is constrained by a Courant number less than unity. The force is obtained based on

$$\boldsymbol{F} = \oint (p\boldsymbol{I} + \mu \boldsymbol{R}_{dev}) \cdot \mathrm{d}\boldsymbol{S}, \tag{2.3}$$

where p is the pressure, $\boldsymbol{R}_{dev}$ is the deviatoric Reynolds stress tensor (Jasak 1996), μ is the dynamic viscosity of the fluid and $\boldsymbol{S}$ is the face area vector. The weak-coupling algorithm is applied for VIV simulation, where the fluid and structural domains exchange data once per time step. For more details, including the time step and mesh size independence analysis for the simulation framework, refer to Fu *et al.* (2025*b*). Five numerical simulations are performed at maximum Reynolds numbers Re_m of 13 637, 17 330, 21 876, 28 216, and 32 672 in the present study. Both the experimental and numerical results are processed using the same procedures, as described below.

3. Mean drag properties

The VIV response of a flexible pipe consists of three components: (1) the mean displacement in the IL direction induced by the mean drag, (2) the fluctuating VIV response superimposed on the IL mean displacement with zero mean value which presents the IL VIV response, and (3) the fluctuating VIV response in the CF direction with zero mean value (Huera-Huarte 2006) which presents the CF VIV response. The inverse finite element method (Wu 2011) is applied to reconstruct the spanwise distribution of hydrodynamic forces from strain measurements along the pipe. This approach has been adopted in the VIV community to overcome the practical difficulty of directly measuring distributed hydrodynamic forces on a flexible structure (Huera-Huarte 2025).

Analysis of experimental results reveals a bidirectional distribution of mean IL displacement induced by the mean drag force, as figure 3(a) shows, which is attributed to the bidirectional characteristics of the flow field. This section introduces the characteristics of the mean drag, shear force, and moment, as well as the effects of the flow velocity distribution. In addition, the numerical simulation results are also presented to further strengthen the credibility of the findings.

3.1. *Mean displacement and mean drag coefficient*

Figure 3 illustrates the mean IL displacement A_{mean}/D which is induced by the mean drag, the corresponding flow velocity distribution characterized by the relative Reynolds number Re_r, for the case associated with $U_m = 0.87\,\mathrm{m/s}$, the maximum Reynolds number $Re_m = 2.48 \times 10^4$, and the maximum mean IL displacement $A_{mean,m}/D$ across different test conditions. Here, $A_{mean,m}$ is defined as the spanwise maximum of the magnitude of the local mean IL displacement $A_{mean,m} \equiv \max_{z\in[0,L]} |A_{mean}(z)|$. In figure 3(a), the blue curve represents the flow velocity profile, which displays a bidirectional shear pattern. The velocity reaches its minimum value of $-U_m$ at $Z = 0$, and increases linearly toward a maximum value of about U_m at $Z = L$. The black curve denotes the mean IL displacement distribution, which exhibits a sinusoidal shape, consistent with the applied flow condition.

Figure 3(b) presents the polynomial fit of the relationship between the maximum mean displacement $A_{mean,m}$ and the flow velocity. The black circles and blue squares represent the experimental and simulation results of the mean displacement, respectively. The fitted curve adopts a quadratic form with a zero intercept from experimental data, expressed as $A_{mean,m}/D = 0.51U_m^2 - 0.05U_m$. The fitting indicates that the second-order term dominates the correlation, suggesting a nonlinear dependence of the mean displacement on the inflow velocity magnitude. The blue squares represent the simulation results, which agree well with the experimental data, exhibiting the same second-order trend.

The mean drag $F_{md}(z)$ is the mean value of force in the IL direction in equation (2.2) as the time average of the drag force as $F_{md}(z) = \langle F_x(z,t)\rangle_t$, and the drag coefficient $C_d(z)$ is expressed as:

$$C_d(z) = \frac{2F_{md}(z)}{\rho D U(z)|U(z)|}, \tag{3.1}$$

where $U(z)$ denotes the local flow velocity at spanwise position z. As shown in figure 3, the maximum mean IL displacement is approximately $1.0D$ as 28.41 mm. Over a segment of length $0.25L$, the corresponding local inclination angle is estimated to be 0.84°, indicating that its influence on the normal-velocity correction is negligible. Therefore, we use $U(z)$ as the reference velocity in equation (3.1). However, it should be noted that this conclusion is only validated over the Reynolds-number range $Re \in [8523, 39\,490]$ in the present study, and a correction would be required for higher Re and larger length-to-diameter ratios.

Figure 4 presents the spanwise distribution of the drag coefficient $C_d(z)$ for six repre-

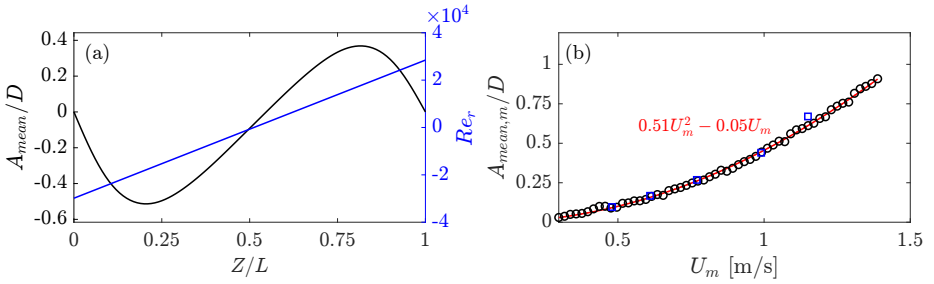

Figure 3: Mean displacement distribution along the pipe and maximum value versus flow velocity: (a) Mean displacement distribution in the IL direction (black line –), relative flow velocity distribution (blue line –) at $U_m = 0.87\,\mathrm{m/s}$ ($Re_m = 2.48 \times 10^4$) based on experimental data. (b) Maximum mean displacement $A_{mean,m}/D$ versus U_m of experiment results (black circle ○) and simulation results (blue square □), fitting result based on U_m (red line –) as $A_{mean,m}/D = 0.51U_m^2 - 0.05U_m$.

sentative cases with increasing flow velocity $U_m = 0.58, 0.73, 0.87, 1.05, 1.21$ and $1.37\,\mathrm{m/s}$. Across all cases, the mirrored curves (red squares, □) closely collapse onto the measurements over most of the span, demonstrating that the spanwise distribution of the mean drag is largely symmetric with respect to the mid-span ($Z/L = 0.5$). In particular, both the averaged value and the spatial variation trend of $C_d(z)$ are well reproduced by the mirrored profiles, which indicates that the drag coefficient distributions remain consistent when the background velocity direction changes. The mirrored profiles show some small differences from the measurements, mainly occurring in the mid-span velocity direction change region and near the two ends, where our experimental boundary condition setup, shown in figure 2, can introduce such small asymmetry over the spanwise direction. In flexible pipe VIV studies, analysis typically focuses on a well-behaved spanwise region with consistent response statistics, while portions affected by end boundary conditions and local singularities are excluded, and this practice also reflects the main VIV region of engineering risers (Trim *et al.* 2005).

Meanwhile, overlaying the spanwise distributions of the VIV response A_{CF}/D and the drag coefficient C_d does not reveal an obvious one-to-one relationship. For example, figures 4(a) and (b) show essentially the same CF response shape but different C_d distributions, and a similar observation can be made by comparing figures 4(c) and (d). In flexible pipe VIV analysis, it is therefore more common to examine relationships based on spanwise-averaged quantities as discussed below.

Figure 5(a) presents the spanwise distribution of the drag coefficient C_d for the case of $U_m = 1.19\,\mathrm{m/s}$. Only the two valid regions ($0.1 \leqslant Z/L \leqslant 0.4$ and $0.6 \leqslant Z/L \leqslant 0.9$) are reported: measurements near the two ends are excluded due to end effects, whereas the central region is omitted because the extremely low local flow velocity yields unrealistically large C_d values from equation (3.1), as shown in figure 4. Within the retained regions, C_d fluctuates around its spanwise-averaged value. Moreover, the close agreement between the original and mirrored distributions supports the use of a near-symmetric mean-drag assumption in the subsequent analysis.

Figure 5(b) shows the mean drag coefficient C_{dm}, defined as the spanwise-average drag coefficient $C_{dm} = \langle C_d(z)\rangle_Z$, which is averaged over the selected spanwise regions shown in figure 5(a). The values of C_{dm} remain nearly constant across cases with different Reynolds numbers Re_m. To quantify this trend, we further compute the average value over all N test conditions within $Re_m \in [8523, 39\,490]$ in figure 5(b) as $\overline{C_{dm}} = \frac{1}{N}\sum_{n=1}^{N} C_{dm}^{(n)}$, where $C_{dm}^{(n)}$ denotes the mean drag coefficient of the nth test condition. Here, we obtain $\overline{C_{dm}} = 1.47$ for the present study based on experimental data as shown in figure 5(b). The blue squares denote

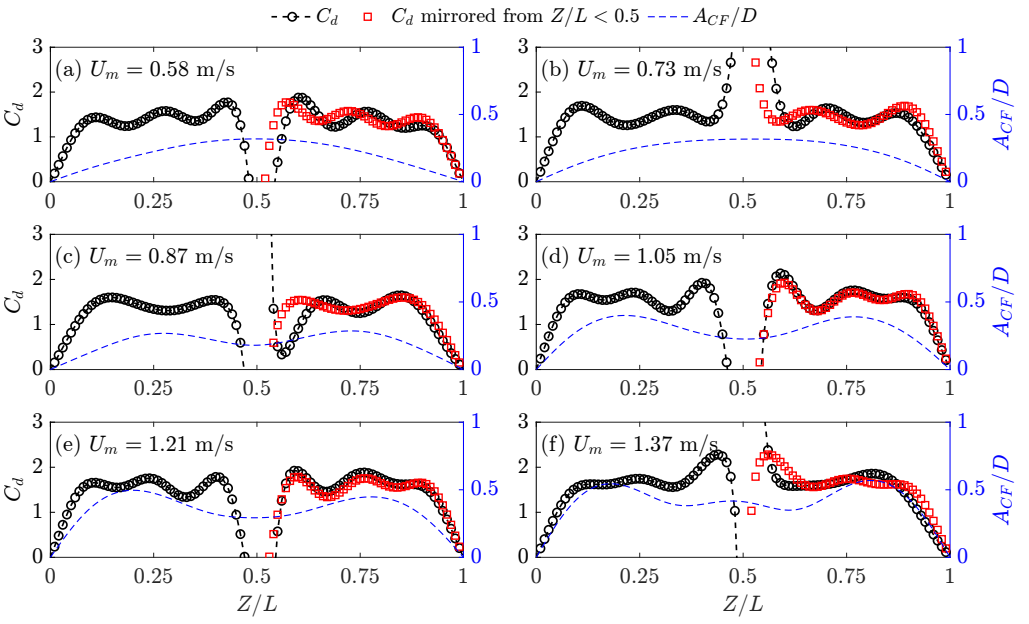

Figure 4: Drag coefficient C_d (black circle with dash line −○−) , mirrored drag coefficient from $Z/L < 0.5$ (red square □), and nondimensional root-mean-square displacement in the CF direction A_{CF}/D (blue dashed line - -) of different cases based on experimental data: (a) $U_m = 0.58\,\mathrm{m/s}$ ($Re_m = 1.65 \times 10^4$), (b) $U_m = 0.73\,\mathrm{m/s}$ ($Re_m = 2.07 \times 10^4$), (c)$U_m = 0.87\,\mathrm{m/s}$ ($Re_m = 2.47 \times 10^4$), (d) $U_m = 1.05\,\mathrm{m/s}$ ($Re_m = 2.98 \times 10^4$), (e) $U_m = 1.21\,\mathrm{m/s}$ ($Re_m = 3.44 \times 10^4$), and (f) $U_m = 1.37\,\mathrm{m/s}$ ($Re_m = 3.89 \times 10^4$).

simulation results processed using the same procedure as the experimental data stated above and show good agreement with the measurements.

We further investigate the relation between the drag coefficient and the VIV displacement magnitude by plotting the maximum root-mean-square CF displacement amplitude along the spanwise direction $A_{CF,max}/D$ in figure 5(b). Here, figure 5(b) shows that the mean drag coefficient of a flexible pipe under bidirectionally sheared flow exhibits limited sensitivity to changes in Re_m, even though the VIV response amplitude in the CF direction displays an amplitude jump phenomenon when increasing Re_m. This suggests that there is no clear relationship between the mean drag coefficient and VIV amplitude subject to bidirectionally sheared flow. This behavior differs from that observed in uniform flow, where the span-averaged drag coefficient C_{dm} is generally found to be strongly correlated with the CF vibration amplitude. For example, Vandiver (1983) proposed the empirical relation $C_{dm} = C_{d0}[1 + 1.043(2A_{CF,max}/D)^{0.65}]$, and Jhingran *et al.* (2008) subsequently extended this approach to sectional drag coefficients as $C_d(z) = C_{d0}[1 + 1.043(2A_{CF}(z)/D)^{0.65}]$, where C_{d0} is the stationary bluff cylinder drag coefficient under same Re. However, in bidirectionally sheared flow VIV, we found that the mean drag coefficient C_{dm} does not display an obvious correlation with the maximum RMS displacement $A_{CF,max}$ in the CF direction shown in figure 5(b), and the sectional drag coefficient $C_d(z)$ does not show a clear dependence on local response displacement $A_{CF}(z)$ shown in figure 4. Instead, the trend between C_{dm} and Re_m in figure 5(b) is consistent with the linearly sheared flow results (Song *et al.* 2016*b*), where the drag coefficient was found to be relatively insensitive to Reynolds number for $Re > 5\times10^4$. This agreement suggests that the reversal of flow direction has a negligible influence on the mean drag coefficient within the Reynolds number range

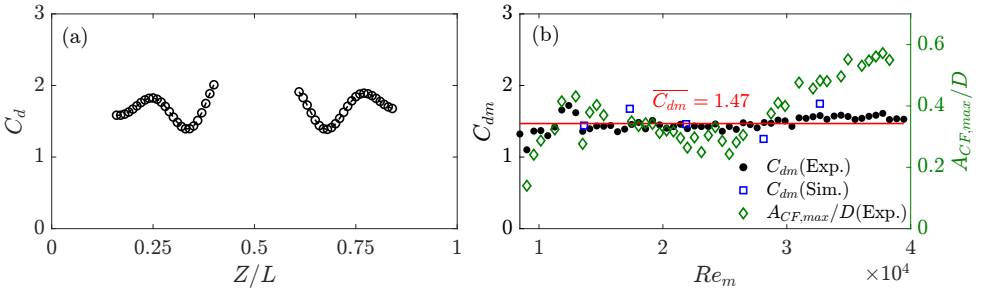

Figure 5: Drag coefficient C_d along the pipe and the mean drag coefficient C_{dm} with different Re_m cases: (a) Drag coefficient (black circle with dashed line $-\circ-$) at $U_m = 1.19\,\mathrm{m/s}$ ($Re_m = 3.38 \times 10^4$) for $Z/L \in [0.1, 0.4] \cup [0.6, 0.9]$ based on experimental data. (b) Mean drag coefficient versus Re_m of experimental results (black circle $\circ$) and simulation results (blue square $\square$), maximum root-mean-square CF displacement along the spanwise direction from Fu *et al.* (2022*a*) (green diamond $\diamond$) and the mean value of mean drag coefficient of all experimental cases $\overline{C_{dm}} = 1.47$ (red line $-$).

considered here. The mean drag coefficient $\overline{C_{dm}} = 1.47$ averaged across different Re_m is performed using the experimental data in the present study due to greater credibility.

3.2. *Shear force and moment*

The drag coefficients on both sides of the flexible pipe are similar, whereas the flow velocities are opposite, resulting in the generation of opposing drag forces. Consequently, the flexible pipe can be considered to experience a pair of forces acting in opposite IL directions with a shear force distribution, resulting in an antisymmetric mean displacement distribution, as shown in figure 3 (a).

The shear force distribution $V(z)$ is obtained by integrating the distributed force $F_{md}(z)$ along the pipe and subtracting both the total force and the first-order moment as (Clough & Penzien 2003):

$$V(z) = \int_0^L F_{md}(\zeta)\mathrm{d}\zeta - \frac{1}{L}\int_0^L F_{md}(\zeta)\zeta\mathrm{d}\zeta - \int_0^z F_{md}(\zeta)\mathrm{d}\zeta, \tag{3.2}$$

and then the bending moment distribution $M(Z)$ is

$$M(z) = \int_0^z V(\zeta)\mathrm{d}\zeta. \tag{3.3}$$

Figure 6(a) presents the shear force distribution $V(z)$ of case $U_m = 0.87\,\mathrm{m/s}$ ($Re_m = 24\,717$). The positive shear force maximum V_{max} appears near the midpoint of the pipe in the cases of bidirectionally sheared flow, as figure 6(a) shows, which is different from the classical uniformly loaded beam, where the shear force vanishes at the center. For a uniformly loaded beam, the shear force is zero at the midpoint and reaches its maximum magnitude at the supports on both ends (Clough & Penzien 2003). This distribution is analogous to the drag force conditions under uniform and linearly sheared flows, where the force exerted along the structure also follows a spatially varying pattern with shear force extrema near the ends. Figure 6(b) illustrates the relationship between the maximum shear force, V_{max}, and the dimensionless term, $0.5\rho DLU^2$, across all test conditions. A clear linear correlation is evident, with the fitted data yielding a shear force coefficient of $C_s = 0.0619$. Similarly, the solid blue squares represent the simulation results, which agree closely with the experimental data and thereby enhance confidence in the simulations, given that both results are processed using the same procedures.

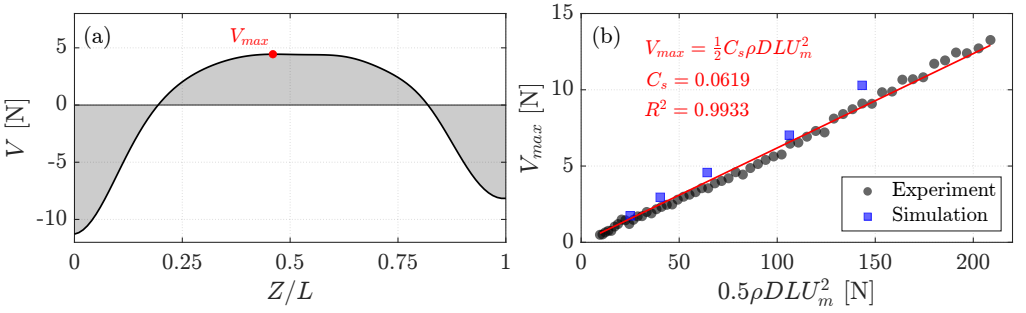

Figure 6: Shear force V along the pipe and the maximum shear force in different cases: (a) Shear force $V(z)$ distribution (black line –) along the pipe at $U_m = 0.87$ m/s ($Re_m = 2.48 \times 10^4$) based on experimental data. (b) Maximum shear force V_{max} in different cases (black dots •), fitting line (red line –) with $V_{max} = \frac{1}{2}C_s\rho DLU_m^2$, $C_s = 0.0619$ based on experiment data, and simulation results (solid blue square ■).

Furthermore, figure 7 illustrates the bending moment distribution based on equation (3.3). Figure 7(a) displays the distribution for a representative case with $U_m = 0.87$ m/s ($Re_m = 24\,717$), revealing a relatively symmetric pattern characterized by two extreme points. The variation $|M|_{max}$ with flow velocity is also analyzed. Using the dimensionless term $0.5\rho DL^2U^2$, curve fitting yields a bending moment coefficient of 0.0159. For vortex-induced vibration of flexible pipes under unidirectional flow (Fu *et al.* 2025*b*), the mean displacement in the IL direction does not exhibit the distinct bidirectional distribution observed under bidirectional shear flow, and no extrema of shear force or bending moment appear in spanwise. The solid blue squares represent the simulation results which agree well with the experimental data.

Based on the above analysis, we draw the following conclusions regarding the first research question posed in § 1:

The bidirectionally sheared inflow introduces a characteristic bidirectional (antisymmetric) mean IL displacement distribution that follows the sign change of the local flow velocity. As shown in figure 3(a), $A_{mean}(z)$ exhibits an approximately sinusoidal spanwise variation, and the spanwise maximum $A_{mean,m}$ increases nonlinearly with the mean inflow magnitude, with a dominant quadratic dependence on U_m, as shown in figure 3(b). In contrast, the corresponding mean drag coefficient distribution remains largely symmetric with respect to the mid-span: the measured $C_d(z)$ is well reproduced by the mirrored profiles over most of the span as shown in figure 4, and the spanwise-averaged value C_{dm} stays nearly constant across the tested *Re* range as shown in figure 5(b).

Because the two spanwise halves experience opposite flow directions but similar drag coefficients, the structure is effectively subjected to two opposing mean drag loadings, leading to a non-classical mean shear-force distribution with a maximum near the mid-span and a bending-moment distribution with two extrema as shown in figures 6 to 7. These extrema identify the locations where the mean load effects are most pronounced, and therefore provide a physically motivated indication of potential damage-prone regions under bidirectionally sheared flow, which is fundamentally different from the unidirectional-flow case where such spanwise extrema of mean shear force and moment do not arise.

3.3. *Flow velocity distribution effect*

As stated in § 2, the bidirectionally sheared flow generated by the circular rotating apparatus is not perfectly symmetric in the experiments, exhibiting an offset of approximately 4.5% with only small variations due to pipe vibration; accordingly, we represent the velocity profile as

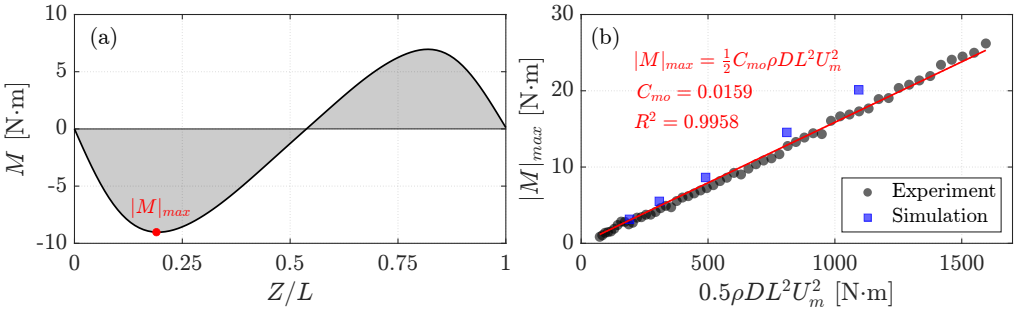

Figure 7: Moment M along the pipe and the maximum absolute value in different cases: (a) Moment M distribution (black line –) along the pipe at $U_m = 0.87$ m/s ($Re_m = 2.48\times10^4$) based on experimental data; (b) Maximum absolute value of moment $|M|_{max}$ in different cases (black dots •), fitting line (red line –) with $|M|_{max} = \frac{1}{2}C_{mo}\rho DL^2U_m^2$, $C_{mo} = 0.0159$ based on experimental data, and simulation results (solid blue square ■).

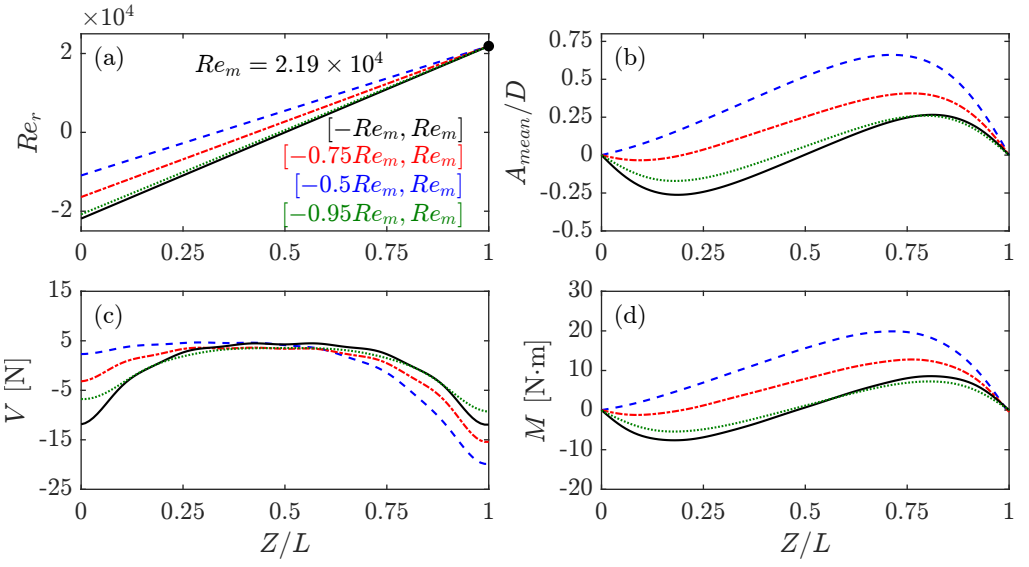

Figure 8: Shear force V and bending moment M with different flow velocity Re_r distributions: (a) Flow relative Reynolds number Re_r distribution, the maximum Reynolds number is fixed as $Re_m = 2.19\times10^4$ with three flow velocity cases by simulation: $Re_r \in [-Re_m, Re_m]$ (black line –), $Re_r \in [-0.75Re_m, Re_m]$ (red dash-dotted line - ·-), and $Re_r \in [-0.5Re_m, Re_m]$ (blue dashed line - -), and one case by experiment: $Re_r \in [-0.95Re_m, Re_m]$ (green dotted line · ·). (b) Mean displacement A_{mean}/D of four cases; (c) Shear force V distribution of four cases; (d) Bending moment M distribution of four cases.

$[-0.95Re_m, Re_m]$. By contrast, the numerical simulations assume a perfectly antisymmetric flow velocity distribution over the spanwise direction. Here, we consider the experimental offset to cross-validate the credibility of the experimental and numerical simulation results, which also provides supporting evidence that our experimental setup can effectively generate the bidirectionally sheared flows. Moreover, numerical simulations are employed to investigate the mean displacement characteristics under two non-symmetric flow velocity distributions to investigate the flow velocity distribution effect.

Figure 8 presents the distributions of the shear force V and bending moment M under

different flow conditions from numerical simulations, characterized by the range of relative Reynolds number $Re_r \in [-Re_m, Re_m]$ (black line –), $Re_r \in [-0.75Re_m, Re_m]$ (red line –), $Re_r \in [-0.5Re_m, Re_m]$ (blue line –), where $Re_m = 2.19 \times 10^4$. Figure 8 also show one case obtained from the experiment with $Re_r \in [-0.95Re_m, Re_m]$ (green dotted line · ·). As shown in figure 3, the experimental distribution of A_{mean}/D is not perfectly antisymmetric because the imposed velocity profile contains a small offset as described in § 2, whereas the numerical results exhibit perfect symmetry by construction. Despite this difference, the experimental and numerical results agree well in overall magnitude, including the extreme values of all three response parameters A_{mean}, V, and M as shown in figure 8(b-d). It should also be noted that, due to limitations of the current experimental setup, real-time measurement of the velocity profile offset is not yet feasible; therefore, treating the experimental velocity profile as antisymmetric in future studies is a reasonable approximation. Here, figure 8(a) shows the flow velocity distribution, and figure 8(b) shows the corresponding mean displacement distribution. As the magnitude of flow velocity at $Z/L = 0$ decreases, the antisymmetric pattern of mean displacement gradually diminishes. When the flow velocity on one side is reduced to half (blue lines), the opposite mean displacement shape disappears (figure 8b), and the resulting displacement distribution resembles that induced by unidirectional linearly sheared flow (Song *et al.* 2016*a*).

Figures 8(c) and (d) show the shear force and bending moment distributions of these cases. It is observed that as the edge flow velocity at $Z/L = 0$ decreases, the shear force value at the corresponding end is reduced. However, the central shear force extrema remain comparable to those under bidirectionally sheared flow with $Re_r \in [-Re_m, Re_m]$, even when the magnitude of the edge velocity is reduced to $0.5Re_m$. In contrast, figure 8(d) shows that the bending moment significantly changes. The antisymmetric bending moment distribution, which resembles the mean displacement pattern, transitions to a profile similar to the linearly sheared flow case when the magnitude of the edge velocity is reduced to $0.5Re_m$.

4. VIV hydrodynamic properties

In this section, we analyze the VIV hydrodynamic properties based on the numerical simulation results, using the distributed response along the pipe length for hydrodynamic identification. Flow field measurements were not conducted in the present experiments due to practical limitations associated with the long test pipe and the rotating towing apparatus. The inverse finite element method (Wu 2011; Song *et al.* 2016*a*) is applied to reconstruct the spanwise distribution of hydrodynamic forces. This inverse identification method can produce the continuous force distribution and has been validated with CFD strip force results. The force decomposition introduced later is then applied to obtain the corresponding force components. Previous experimental studies have demonstrated that the flexible pipe VIV exhibits pronounced multi-frequency response behavior (Bourguet *et al.* 2012, 2013; Ma *et al.* 2022), which becomes more evident in bidirectionally sheared flow (Fu *et al.* 2022*a*,*c*). Conventional least squares (Wu 2011), energy-based (Wang *et al.* 2021*a*), and Fourier series (Fan *et al.* 2019*a*) methods have been shown to inadequately capture the hydrodynamic characteristics of VIV with multi-frequency responses. The forgetting-factor least squares method is then employed for the effective identification of multi-frequency VIV hydrodynamics (Liu *et al.* 2018, 2020; Fu *et al.* 2024).

For flexible pipes, the dominant frequency VIV remains the primary concern, as it often contributes most significantly to fatigue damage (Baarholm *et al.* 2006). This section first analyzes the hydrodynamic forces associated with dominant VIV under bidirectionally sheared flows, followed by an investigation of the time-varying VIV hydrodynamic response.

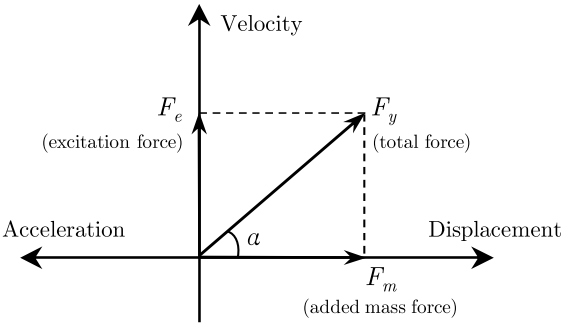

Figure 9: Illustration of the VIV force decomposition in equation (4.1). The total force F_y is decomposed into two components: F_e, the excitation force that is in phase with the velocity and represents the fluid excitation associated with VIV; and F_m, the added-mass force that is in phase with the acceleration and represents the instantaneous added-mass contribution.

4.1. *Dominant frequency VIV hydrodynamic properties*

The VIV hydrodynamic force can be decomposed into the excitation force F_e, which is in phase with velocity and represents the energy exchange between the structure and the fluid, and the added mass force F_m, which is in phase with acceleration and reflects the added mass effect (Sarpkaya 1995):

$$F_y(z,t) = \underbrace{\frac{1}{2\sqrt{2}\dot{\xi}_{y,\mathrm{rms}}(z)}\rho D U^2(z) C_e(z,t)\dot{\xi}_y(z,t)}_{F_e} \underbrace{- \frac{\pi D^2}{4}\rho C_m(z,t)\ddot{\xi}_y(z,t)}_{F_m}, \tag{4.1}$$

where C_e is the excitation coefficient and C_m is the added mass coefficient. This force decomposition has been widely used in engineering practice to support VIV prediction. To obtain the dominant frequency component of the hydrodynamic force, we apply the band-pass filter with a range of 0.8 to 1.2 times the sectional vibration dominant frequency obtained from the peak of the power spectral density. Figure 9 schematically illustrates the VIV force decomposition adopted in equation (4.1). The CF hydrodynamic force F_y is expressed as the sum of two components: an excitation force F_e and an added-mass force F_m. Here, the excitation force F_e is in phase with the transverse velocity and quantifies the portion of the fluid force responsible for energy exchange with the structure. The added-mass force F_m is in phase with the transverse acceleration and represents the instantaneous added-mass contribution. By projecting F_y onto these two orthogonal directions, figure 9 provides a geometric interpretation of how the total VIV force is partitioned between the energy-input mechanism F_e and the added-mass mechanism F_m. The angle α characterizes the relative phase of the resultant force in this reference frame.

For the dominant hydrodynamic force $\hat{\boldsymbol{F}}_{\boldsymbol{y}}$ in spatial and temporal distributions, we have:

$$\hat{\boldsymbol{F}}_{\boldsymbol{y}} = \overset{\text{Spanwise Location}\ \longrightarrow}{\begin{bmatrix} \hat{F}_y(z_1,t_1) & \hat{F}_y(z_2,t_1) & \cdots & \hat{F}_y(z_n,t_1) \\ \hat{F}_y(z_1,t_2) & \hat{F}_y(z_2,t_2) & \cdots & \hat{F}_y(z_n,t_2) \\ \vdots & \vdots & \ddots & \vdots \\ \hat{F}_y(z_1,t_m) & \hat{F}_y(z_2,t_m) & \cdots & \hat{F}_y(z_n,t_m) \end{bmatrix}_{m\times n,}} \Big\downarrow \text{Time} \tag{4.2}$$

where $\hat{(\cdot)}$ represents the dominant frequency part obtained by band-pass filter, $\hat{\boldsymbol{F}}_{\boldsymbol{y}}$ is an $m \times n$ matrix, n represents the number of spanwise locations and m denotes the number of time

steps. Then we have the matrix $\boldsymbol{A}$ as:

$$\boldsymbol{A}=\underbrace{\overbrace{\begin{bmatrix} \mathcal{E}(z_1)\hat{\tilde{\xi}}_y(z_1,t_1) & \mathcal{M}(z_1)\hat{\tilde{\xi}}_y(z_1,t_1) & \cdots & \mathcal{E}(z_n)\hat{\tilde{\xi}}_y(z_n,t_1) & \mathcal{M}(z_n)\hat{\tilde{\xi}}_y(z_n,t_1) \\ \mathcal{E}(z_1)\hat{\tilde{\xi}}_y(z_1,t_2) & \mathcal{M}(z_1)\hat{\tilde{\xi}}_y(z_1,t_2) & \cdots & \mathcal{E}(z_n)\hat{\tilde{\xi}}_y(z_n,t_2) & \mathcal{M}(z_n)\hat{\tilde{\xi}}_y(z_n,t_2) \\ \vdots & \vdots & \ddots & \vdots & \vdots \\ \mathcal{E}(z_1)\hat{\tilde{\xi}}_y(z_1,t_m) & \mathcal{M}(z_1)\hat{\tilde{\xi}}_y(z_1,t_m) & \cdots & \mathcal{E}(z_n)\hat{\tilde{\xi}}_y(z_n,t_m) & \mathcal{M}(z_n)\hat{\tilde{\xi}}_y(z_n,t_m) \end{bmatrix}}^{\text{Spanwise Location}}}_{m\times 2n,}\ \Big\downarrow \text{Time}$$

z_1 location $\qquad$ z_n location

(4.3)

the size of $\boldsymbol{A}$ is $m \times 2n$, and $\mathcal{E}(z)$ and $\mathcal{M}(z)$ are the excitation and added mass force non-dimensional items, respectively:

$$\mathcal{E}(z)=\frac{\rho D U^2(z)}{2\sqrt{2}\,\hat{\tilde{\xi}}_{y,\mathrm{rms}}(z)},\quad \mathcal{M}(z)=-\frac{\rho\pi D^2}{4}. \tag{4.4}$$

Considering equation (4.1) for the dominant hydrodynamic force, the hydrodynamic coefficients at location z_j $(j = 1, 2, \cdots, n)$ can be expressed as $C_e(z_j)$ and $C_m(z_j)$. Then we have:

$$\hat{\mathcal{F}}_y(z_j)=\mathcal{A}(z_j)C(z_j), \tag{4.5}$$

where $\hat{\mathcal{F}}_y(z_j)$ is the dominant CF force of location z_j in time domain which is j^{th} column of $\hat{\boldsymbol{F}}_{\boldsymbol{y}}$ in equation (4.2) with size of $m \times 1$, $\mathcal{A}(z_j)$ is the non-dimensional matrix at location z_j which is $(2j-1)^{\text{th}}$ and $(2j)^{\text{th}}$ column of $\boldsymbol{A}$ in equation (4.3) with size of $m \times 2$. $C(z_j)$ is the hydrodynamic coefficient matrix with a size of 2×1:

$$C(z_j)=\begin{bmatrix} C_e(z_j) \\ C_m(z_j) \end{bmatrix}_{2\times 1}, \tag{4.6}$$

then we have hydrodynamic coefficients at the z_j location based on least squares regression as follows:

$$C(z_j)=\left(\mathcal{A}^{\top}(z_j)\mathcal{A}(z_j)\right)^{-1}\mathcal{A}^{\top}(z_j)\hat{\mathcal{F}}_y(z_j), \tag{4.7}$$

and the spanwise distribution of hydrodynamic coefficients can be obtained by traversing the spanwise location. The following linearly sheared flow and uniform flow cases are taken from Fu *et al.* (2025*b*).

Figure 10 presents the simulation results for a unidirectional linearly sheared flow case with $U_m = 0.80\,\mathrm{m/s}$. All panels are generated from the simulation data, and additional details are provided in Fu *et al.* (2025*b*). Figure 10(a) shows the nondimensional mean displacement A_{mean}/D and the root-mean-square CF and IL response amplitudes, A_{CF}/D and A_{IL}/D, respectively. Figure 10(b) shows the phase difference between IL and CF directions, expressed as:

$$\phi_{xy}(z,t)=\left[\phi_x(z,t)-\frac{\hat{f}_x(z,t)}{\hat{f}_y(z,t)}\phi_y(z,t),\quad \mathrm{mod}\ 360^\circ\right], \tag{4.8}$$

where $\phi_x(z,t)$ and $\phi_y(z,t)$ are the instantaneous phases of the dominant IL and CF response, respectively, as

$$\begin{aligned} \phi_x(z,t)&=\arg\left(\hat{\tilde{\xi}}_x(z,t)+\mathrm{i}\mathcal{H}(\hat{\tilde{\xi}}_x(z,t))\right), \\ \phi_y(z,t)&=\arg\left(\hat{\tilde{\xi}}_y(z,t)+\mathrm{i}\mathcal{H}(\hat{\tilde{\xi}}_y(z,t))\right), \end{aligned} \tag{4.9}$$

where $\mathcal{H}$ represents the Hilbert transform, and $\hat{f}_x(z,t)$ and $\hat{f}_y(z,t)$ represent the instanta-

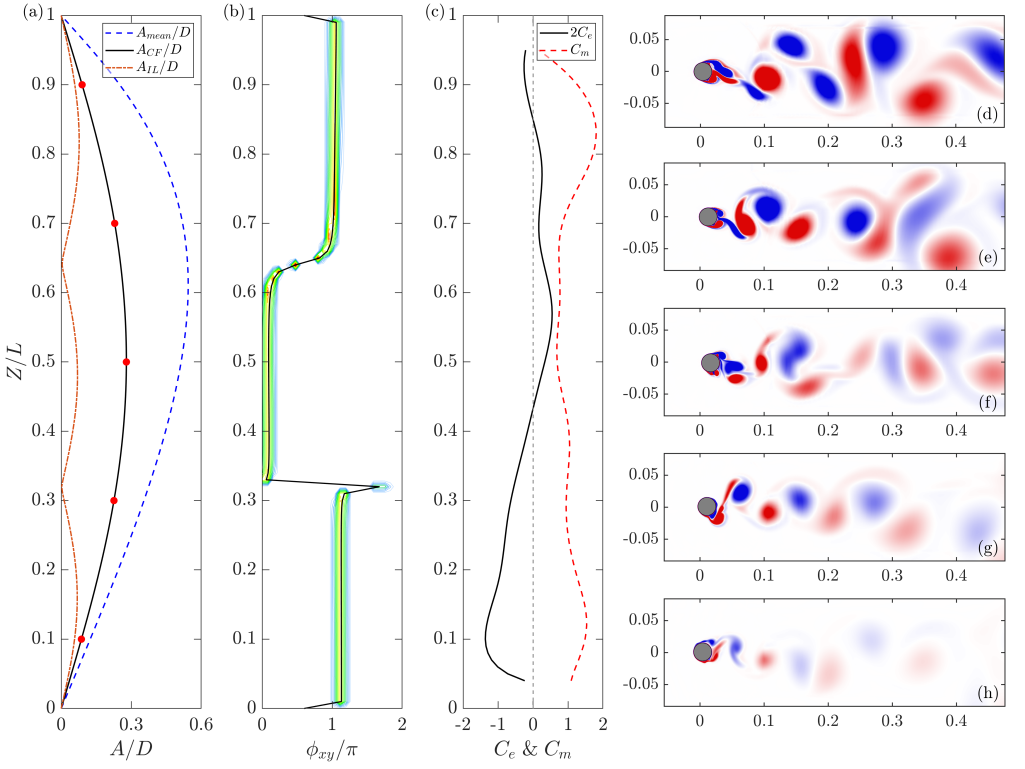

Figure 10: Dominant hydrodynamic properties along the pipe of the linearly sheared flow case $U_m = 0.80\,\mathrm{m/s}$ ($Re_m = 2.27 \times 10^4$) with unidirectional flow distribution based on numerical simulation data: (a) Spanwise distribution of VIV response of mean displacement (blue dashed line - -), IL (orange dash-dotted line -·-) and CF (black line –) RMS displacement. (b) Histogram of phase difference ϕ_{xy}, where a selected moment of phase difference is presented in black line (–). (c) Excitation (black line –) and added mass (red dashed line - -) coefficient distributions. (d) to (h) Instantaneous vorticity contours ω_z correspond to the red circular dots (•) in subfigure (a) of locations of $Z/L = 0.0256, 0.2632, 0.4737, 0.6842$ and 0.8947 with coordinates plotted in meters. Blue to red: negative to positive values with fixed $[-30, 30]$ range.

neous dominant response frequencies at different spanwise locations obtained based on the local maxima of the wavelet transform magnitude. Let $\mathcal{W}[\hat{\xi}_x](z,t,f)$ and $\mathcal{W}[\hat{\xi}_y](z,t,f)$ denote the wavelet transform of the dominant response in the IL and CF directions. Then, the instantaneous dominant frequencies are defined as (Lilly & Olhede 2012):

$$\hat{f}_x(z,t) = \arg\max_f \left|\mathcal{W}[\hat{\xi}_x](z,t,f)\right|, \quad \hat{f}_y(z,t) = \arg\max_f \left|\mathcal{W}[\hat{\xi}_y](z,t,f)\right|, \tag{4.10}$$

where $\hat{f}_x(z,t)$ and $\hat{f}_y(z,t)$ represent the instantaneous dominant frequencies in the in-line and cross-flow directions, respectively, obtained by identifying the frequency corresponding to the maximum wavelet transform magnitude at each spanwise location z and time t, and the phase difference of select time is shown in black line. Figure 10(c) presents the hydrodynamic coefficients determined by equation (4.7), whereas figure 10(d)-(h) show the contour of $\omega_z = \partial v/\partial x - \partial u/\partial y$ within the range $[-30, 30]$, corresponding to the red dots highlighted in figure 10(a) with locations of $Z/L = \frac{1}{19}, \frac{5}{19}, \frac{9}{19}, \frac{13}{19}$ and $\frac{17}{19}$. It should be noted that the results in this section are illustrated based on simulation results.

In the linearly sheared flow case, the maximum velocity occurs at $Z/L = 1$. As shown in

figure 10, the mean displacement exhibits an asymmetric distribution, with larger displacements observed in regions subjected to higher flow velocities. The CF direction is dominated by the first mode response, whereas the IL direction is dominated by the third mode response. A phase jump is observed at the nodes in the IL direction. The hydrodynamic coefficients exhibit stochastic behavior. The hydrodynamic coefficient C_e, associated with the dominant mode of the flexible pipe, is generally correlated with the motion trajectory (Fan *et al.* 2019*b*), whereas C_m is typically related to the wake pattern (Wang *et al.* 2021*a*). The response characteristics of the flexible pipe become more complex under bidirectionally sheared flow. This study aims to analyze the hydrodynamic properties, with a particular emphasis on evaluating whether the hydrodynamic behavior of a flexible pipe in a bidirectional flow field resembles that in a unidirectional flow field. Figure 11 presents the simulation results of the dominant VIV result under uniform flow of $U = 1.4\,\mathrm{m/s}$ ($Re = 4.34 \times 10^4$). The mean IL displacement exhibits a symmetric distribution around the midpoint, and the phase jump phenomenon is also discovered in the IL VIV displacement node. The spatial distribution of hydrodynamic coefficients likewise reveals more complex variations with higher order VIV. It can also be observed that the uniform-flow case exhibits a more pronounced mean IL displacement shown in figure 11(a). The maximum mean IL displacement exceeds $5.0D$, which shifts the cylinder substantially from its original position in the vorticity contours. In contrast, for the subsequent bidirectionally sheared flow case, the mean IL displacement remains below $1.0D$.

Figure 12 to figure 14 present the dominant hydrodynamic properties of the bidirectionally sheared flow cases $U_m = 0.61\,\mathrm{m/s}$, $0.99\,\mathrm{m/s}$ and $1.15\,\mathrm{m/s}$ with Re_m corresponding to 1.73×10^4, 2.81×10^4 and 3.27×10^4, respectively. All panels are generated based on numerical simulation data. The low velocity region near the midpoint is omitted. Taking the bidirectionally sheared flow condition with $U_m = 0.61\,\mathrm{m/s}$ as an example, as shown in figure 12, it has been previously demonstrated in figure 3 that the mean displacement of the flexible riser in the IL direction exhibits an antisymmetric pattern under bidirectionally sheared flow. An analysis of the influence of the background current profile on the phase difference of the dominant mode reveals that, for VIV under bidirectionally sheared flow, the phase difference generally exhibits an antisymmetric distribution around the midpoint (Wang *et al.* 2021*b*). Phase jumps continue to occur at the nodes of the IL-dominated mode, with a phase shift of approximately π between adjacent regions along the pipe, maintaining an antisymmetric pattern around the midpoint. The dominant mode phase distribution is relevant for semi-empirical prediction studies. The observed phase difference patterns between the dominant CF and IL responses offer valuable insights for guiding future research.

Similarly, under bidirectionally sheared flows with $U_m = 0.99\,\mathrm{m/s}$ ($Re_m = 2.81 \times 10^4$) and $U_m = 1.15\,\mathrm{m/s}$ ($Re_m = 3.27 \times 10^4$) (as shown in figure 13 and figure 14), the phase difference exhibits a variation similar to that observed at $U_m = 0.61\,\mathrm{m/s}$. As the flow velocity further increases, for the case of $U_m = 0.99\,\mathrm{m/s}$, a phase jump of π is still observed at the IL nodes; however, a more complex phase transition appears near the mid-span of the model (as shown in figure 13). The cases of $U_m = 0.99\,\mathrm{m/s}$ and $U_m = 1.15\,\mathrm{m/s}$ exhibit similar phase variation patterns, with the phase difference distribution remaining antisymmetric about the structural midpoint under bidirectionally sheared flow induced VIV.

Further investigations are conducted on the distributions of the excitation force coefficient and the added mass coefficient along the riser. Due to the unique antisymmetric velocity profile of the bidirectionally sheared flow, whether the excitation force coefficient C_e exhibits symmetry about the midpoint determines the feasibility of approximating the flow field using a symmetric unidirectional profile (by taking the absolute value of the bidirectional shear flow velocity) for engineering predictions. For the cases discussed in this study, the distribution of the excitation force coefficient generally displays an approximately symmetric pattern

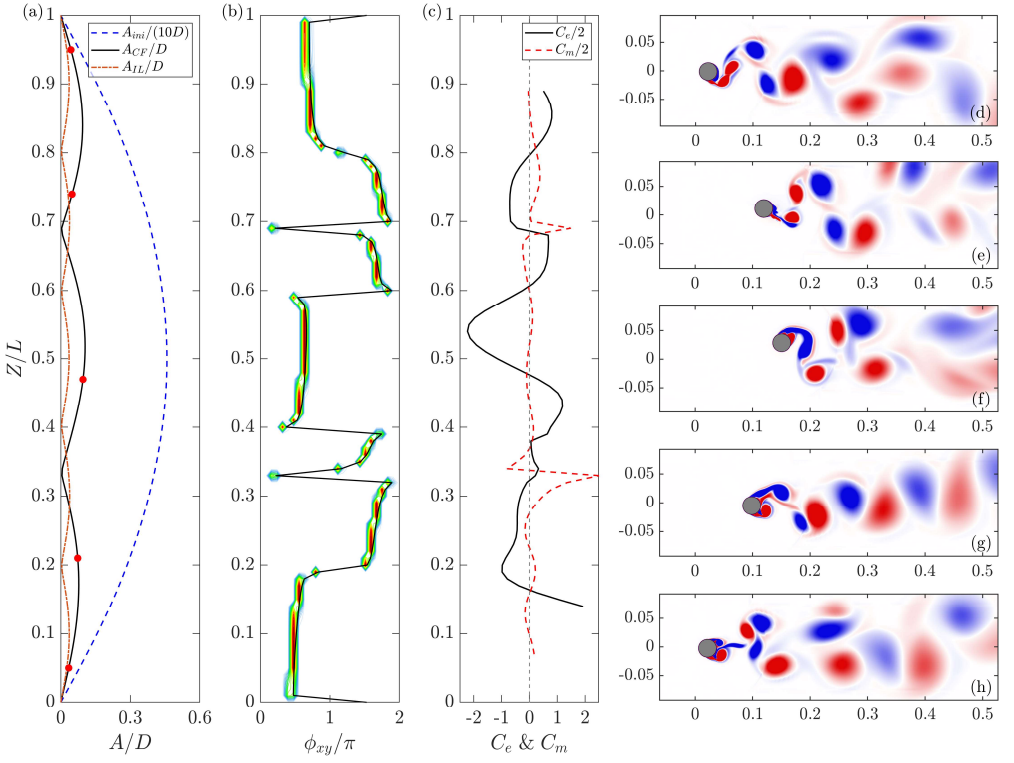

Figure 11: Dominant hydrodynamic properties along the pipe of the uniform flow case U_m = 1.40 m/s ($Re_m = 4.34 \times 10^4$) with unidirectional flow distribution based on numerical simulation data: (a) Spanwise distribution of VIV response of mean displacement (blue dashed line - -), IL (orange dash-dotted line -·-) and CF (black line –) RMS displacement. (b) Histogram of phase difference ϕ_{xy}, where a selected moment of phase difference is presented in black line (–). (c) Excitation (black line –) and added mass (red dashed line - -) coefficient distributions. (d) to (h) Instantaneous vorticity contours ω_z correspond to the red circular dots (•) in subfigure (a) with coordinates plotted in meters. Blue to red: negative to positive value with fixed $[-96, 96]$ range.

about the midpoint, although strict symmetry is not observed. For example, in figure 12(c), the excitation coefficients at both sides exhibit a distribution pattern resembling that of a third-mode like response, characterized by positive-negative-positive symmetry. A similar distribution is observed in figure 13(c). In figure 14(c), this symmetric variation pattern becomes even more pronounced, with the excitation force coefficient reaching an extreme value of -1. Nevertheless, the patterns near the mid-span boundaries ($Z/L = 0.65$ and $Z/L = 0.35$) are not completely identical. In the dominant frequency VIV, the added mass coefficients are not always correlated with wake pattern. For the unidirectional linearly sheared flow case shown in figure 10, subfigure (d) displays a P+S wake pattern associated with the negative C_m, while the other subfigures exhibit 2S wake patterns with occasional third small vortex and corresponding positive C_m values. The high-order uniform flow VIV case does not exhibit a hydrodynamic region with a relatively constant value in figure 11. For bidirectionally sheared flow induced VIV, a pronounced traveling wave phenomenon is observed, and the hydrodynamic force distribution exhibits clear temporal variations. The hydrodynamic characteristics at the dominant frequency are not fully correlated with the wake pattern, shown in supplementary movie 1 for the linearly sheared flow case with

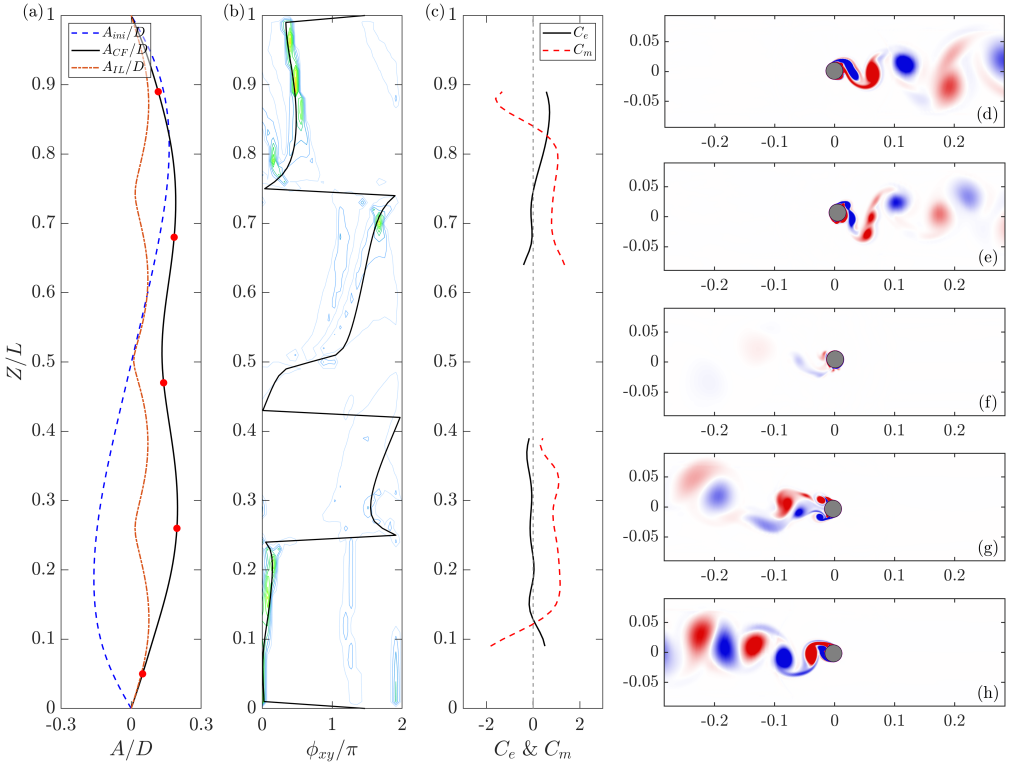

Figure 12: Dominant hydrodynamic properties along the pipe of the bidirectionally sheared flow case $U_m = 0.61\,\mathrm{m/s}$ ($Re_m = 1.73 \times 10^4$) based on numerical simulation data: (a) Spanwise distribution of VIV response of mean displacement (blue dashed line - -), IL (orange dash-dotted line -·-) and CF (black line –) RMS displacement. (b) Histogram of phase difference ϕ_{xy}, where a selected moment of phase difference is presented in black line (–). (c) Excitation (black line –) and added mass (red dashed line - -) coefficient distributions. (d) to (h) Instantaneous vorticity contours ω_z correspond to the red circular dots (•) in subfigure (a) with coordinates plotted in meters. Blue to red: negative to positive value with fixed $[-40, 40]$ range.

$U_m = 0.80\,\mathrm{m/s}$ and in supplementary movie 2 for the bidirectionally sheared flow case with $U_m = 0.99\,\mathrm{m/s}$. However, figures 12 to 14 indicate that, at both ends of the pipe, the wake patterns exhibit consistent variation with the added mass coefficient at the dominant frequency; the negative C_m corresponds to P+S or 2P wake patterns. The time-varying hydrodynamic properties will be illustrated in the next section.

In general, the added mass coefficient C_m of a flexible pipe undergoing vortex-induced vibration tends to remain close to 1.00 throughout most of its length, which leads to the choice for the engineering prediction (Wu *et al.* 2023). In the figure 10 and figure 12 of the low mode VIV presented in the previous section, the added mass coefficient in the dominant mode remains close to unity along a large portion of the pipe length.

Spectral proper orthogonal decomposition (SPOD) is applied in the present study to analyze the dominant frequency connection between the flow field and flexible pipe (Sieber *et al.* 2016; Towne *et al.* 2018). The approach used in the present study is the one described by Towne *et al.* (2018). Here, we apply SPOD to the flexible pipe VIV wake based on numerical simulation data to identify the dominant frequency components and associated

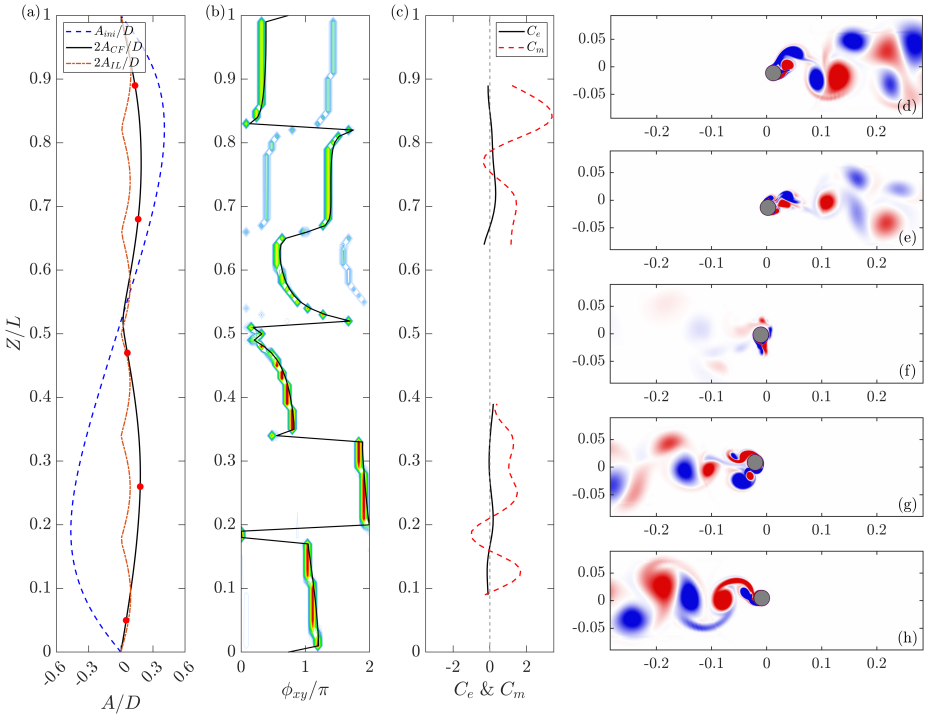

Figure 13: Dominant hydrodynamic properties along the pipe of the bidirectionally sheared flow case $U_m = 0.99\,\mathrm{m/s}$ ($Re_m = 2.81 \times 10^4$) based on numerical simulation data: (a) Spanwise distribution of VIV response of mean displacement (blue dashed line - -), IL (orange dash-dotted line ---) and CF (black line –) RMS displacement. (b) Histogram of phase difference ϕ_{xy}, where a selected moment of phase difference is presented in black line (–). (c) Excitation (black line –) and added mass (red dashed line - -) coefficient distributions. (d) to (h) Instantaneous vorticity contours ω_z correspond to the red circular dots (•) in subfigure (a) with coordinates plotted in meters. Blue to red: negative to positive value with fixed $[-40, 40]$ range.

coherent structures. We define the cross-spectral density matrix at frequency f:

$$\boldsymbol{S}(f) = \frac{1}{E}\sum_{n=1}^{E} \hat{\boldsymbol{\omega}}_n(f)\,\hat{\boldsymbol{\omega}}_n(f)^{\dagger}, \tag{4.11}$$

where the matrix $\boldsymbol{S}(f)$ is the cross-spectral density matrix at frequency f, which is constructed by averaging over E overlapping time segments, $\hat{\boldsymbol{\omega}}_n(f)$ denotes the Fourier transform of the nth time window of the spanwise vorticity field $\omega_z(x, y, t)$ at frequency f and $(\cdot)^{\dagger}$ denotes the Hermitian of the argument. The SPOD modes and corresponding energy content are obtained by solving the eigenvalue problem:

$$\boldsymbol{S}(f)\,\boldsymbol{\phi}_j(f) = \lambda_j(f)\,\boldsymbol{\phi}_j(f), \tag{4.12}$$

where $\lambda_j(f) \in \mathbb{R}^+$ is the energy of the j^{th} mode at frequency f, and $\boldsymbol{\phi}_j(f)$ is the spatial structure of the jth SPOD mode at frequency f. The open implementation of the SPOD algorithm is used in the present study (Schmidt & Colonius 2020), and details can be found in the original source code.

Figures 15 and 16 show the SPOD results for bidirectionally sheared flow cases at $U_m = 0.48\,\mathrm{m/s}$ ($Re_m = 1.36 \times 10^4$) and $U_m = 0.99\,\mathrm{m/s}$ ($Re_m = 2.81 \times 10^4$). All panels are

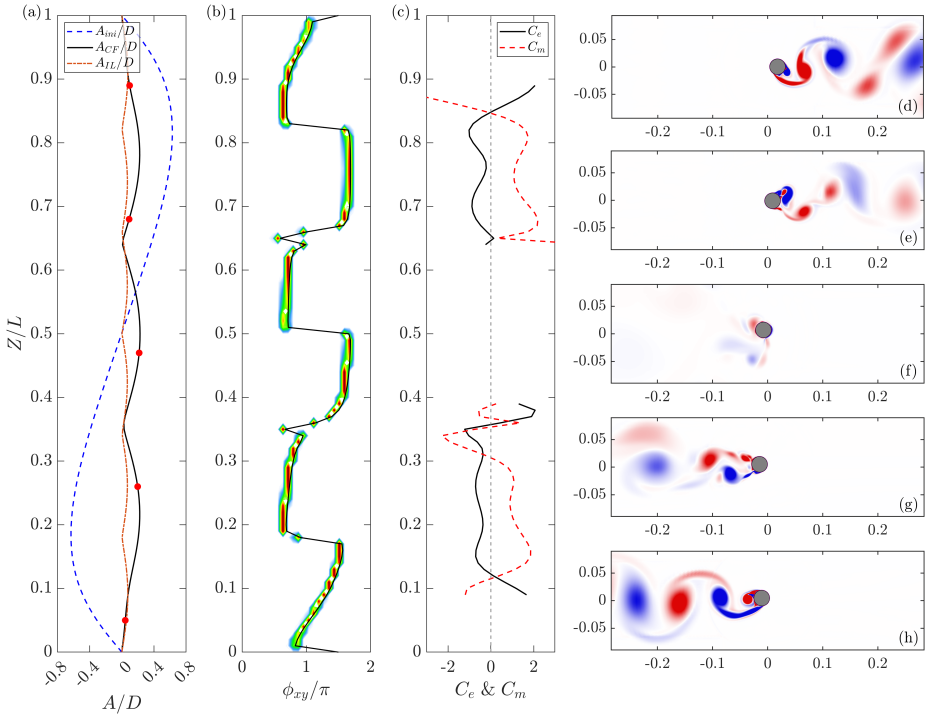

Figure 14: Dominant hydrodynamic properties along the pipe of the bidirectionally sheared flow case $U_m = 1.15\,\mathrm{m/s}$ ($Re_m = 3.27 \times 10^4$) based on numerical simulation data: (a) Spanwise distribution of VIV response of mean displacement (blue dashed line - -), IL (orange dash-dotted line ---) and CF (black line –) RMS displacement. (b) Histogram of phase difference ϕ_{xy}, where a selected moment of phase difference is presented in black line (–). (c) Excitation (black line –) and added mass (red dashed line - -) coefficient distributions. (d) to (h) Instantaneous vorticity contours ω_z correspond to the red circular dots (•) in subfigure (a) with coordinates plotted in meters. Blue to red: negative to positive value with fixed $[-70, 70]$ range.

generated from the simulation data. For the strips at $Z/L = 0.10$ and 0.30, the local flow is from positive to negative, whereas at $Z/L = 0.70$ and 0.90 it is from negative to positive. The nondimensional dominant frequency is defined as $f^* = f_{domi}/f_{c1}$, where f_{domi} denotes the peak frequency and f_{c1} is the first computed natural frequency listed in table 1, and the f^* resolution is about 0.09. In both cases, the first SPOD mode is overwhelmingly dominant, capturing more than 99% of the total modal energy, and its spatial structure is broadly consistent across strips; the key difference lies in how the dominant frequency varies along the flexible pipe.

For the lower-velocity case $U_m = 0.48\,\mathrm{m/s}$ as shown in figure 15, the SPOD peak frequencies in the four strips scale primarily with the local current speed. Specifically, the ratios of the dominant SPOD frequencies are approximately $1 : 0.53 : 0.37 : 0.89$, which are close to the corresponding ratios of the local Strouhal shedding frequencies. We compute local Strouhal shedding frequencies as $0.2U(z)/D$ assuming a Strouhal number of 0.2 (Bourguet *et al.* 2013), which can be estimated as $1 : 0.53 : 0.41 : 0.88$ based on the strip Reynolds numbers ratio. This indicates that, in this regime, the energetic wake dynamics are governed mainly by the local vortex-shedding frequency rather than by the global structural vibration modes.

For the higher-velocity case $U_m = 0.99\,\mathrm{m/s}$ as shown in figure 16, our previous exper-

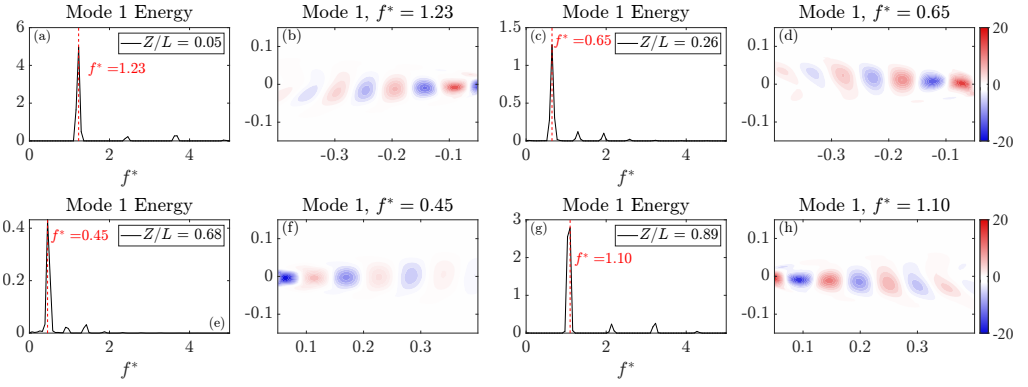

Figure 15: SPOD results at different spanwise locations for the bidirectionally sheared flow case with $U_m = 0.48\,\mathrm{m/s}$ ($Re_m = 1.36 \times 10^4$) based on numerical simulation data. (a), (c), (e), and (g): SPOD mode 1 energy spectra at different $Z/L = 0.0256$, 0.2632, 0.6842, and 0.8947, respectively. The dominant frequency f^* is marked by a red dashed line and labeled above the peak. (b), (d), (f), and (h): First spatial SPOD mode at the corresponding dominant frequency with coordinates plotted in meters. The colorbar range is fixed to $[-20, 20]$ for comparison.

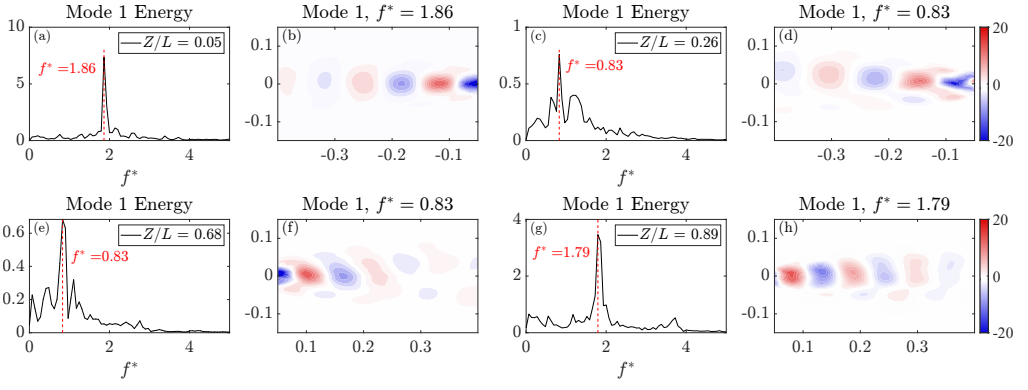

Figure 16: SPOD results at different spanwise locations for the bidirectionally sheared flow case with $U_m = 0.99\,\mathrm{m/s}$ ($Re_m = 2.81 \times 10^4$) based on numerical simulation data. (a), (c), (e), and (g): SPOD mode 1 energy spectra at $Z/L = 0.0256$, 0.2632, 0.6842, and 0.8947, respectively. The dominant frequency f^* is marked by a red dashed line and labeled above the peak. (b), (d), (f), and (h): First spatial SPOD mode at the corresponding dominant frequency with coordinates plotted in meters. The colorbar range is fixed to $[-20, 20]$ for comparison.

imental study (Fu *et al.* 2022*a*) showed that the dominant displacement frequency varies along the span, with the mid-span governed by the first mode and regions near the two ends dominated by the second mode. Here, we have $f^* = 1$ and $f^* = 1.99$ corresponding to the first and second-order structural natural frequencies according to the definition of non-dimensional f^* and their values in Table 1. Consistent with this trend, the SPOD spectra in figure 16 exhibit dominant peaks that cluster near the first-order ($f^* = 1$) and second-order ($f^* = 1.99$) structural natural frequencies, even though the corresponding locations are the same as figure 15 and are not distributed symmetrically. We therefore interpret this higher-velocity regime as a lock-in dominated state, in which the wake dynamics are governed primarily by the structural vibration frequency rather than by the local Strouhal frequency (Bourguet *et al.* 2013).

Moreover, the flexible pipe vibrates in both the IL and CF directions and may exhibit different dominant frequencies in each direction, which can jointly influence the SPOD results. However, CF vibration is typically more important because it has larger amplitudes and contributes more to fatigue damage (Huera-Huarte 2025). Here, the peak frequencies associated with the leading SPOD modes shown in figures 15 and 16 are closely aligned with the dominant response frequency of VIV in the CF direction instead of the IL direction, which indicates that the dominant fluid energy distribution is primarily aligned with the CF vibration pattern. Overall, the SPOD results serve here as supporting evidence for a transition from Strouhal-governed wake dynamics at lower velocity to lock-in governed wake dynamics at higher velocity in bidirectionally sheared flow, and meanwhile SPOD offers an efficient framework for studying the VIV lock-in phenomenon.

Based on the above analysis, we draw the following conclusions regarding the second and third research questions posed in § 1:

(1) *Effect of the antisymmetric velocity distribution on the VIV phase.* The unique antisymmetric velocity distribution of the bidirectionally sheared flow does not alter the phase distribution of the VIV response. A clear phase jump of approximately π is consistently observed at the IL nodes shown in figures 12(b), 13(b), and 14(b), indicating that the fundamental phase jump phenomenon remains unchanged under bidirectionally sheared flow.

(2) *Symmetry of the excitation coefficient at the velocity-reversal point.* The excitation force coefficient C_e exhibits a reasonably symmetric distribution about the flow velocity reversal point, suggesting that the two half-spans contribute in a nearly mirrored distribution shown in figures 12(c), 13(c), and 14(c). This symmetry indicates the potential to simplify a bidirectionally sheared flow case into two separate unidirectional sheared flow cases for engineering prediction purposes.

The property of the added mass coefficient distribution requires further time-domain investigation and will be discussed in the following subsections.

4.2. *Time-varying hydrodynamic properties*

In the previous subsection, the hydrodynamic forces at the dominant frequency were obtained using the least squares method. However, the least squares approach performs poorly in identifying multi-frequency VIV responses and capturing time-varying coefficients (Liu *et al.* 2018). The forgetting-factor least squares (FFLS) algorithm (Fortescue *et al.* 1981) is a variant of least-squares estimation that was originally developed in the adaptive control community. It has been applied in VIV research to identify time-varying hydrodynamic coefficients (Liu *et al.* 2020). Here we define

$$
\begin{aligned}
\boldsymbol{F}_{\boldsymbol{y}}^{*}(z,t_s) &= \boldsymbol{H}_{s}^{*}(z,t_s)\boldsymbol{\theta}_{s}(z,t_s),\\
\boldsymbol{F}_{\boldsymbol{y}}^{*}(z,t_s) &= \left[\beta^{s-1}F_y\left(z,t_1\right),\beta^{s-2}F_y\left(z,t_2\right),\beta^{s-3}F_y\left(z,t_3\right),\cdots,\beta^{0}F_y\left(z,t_s\right)\right]_{s\times 1}^{\top},\\
\boldsymbol{H}_{s}^{*}(z,t_s) &= \left[\begin{array}{cccc}
\beta^{s-1}\mathcal{E}^{*}(z,t_1)\dot{\xi}\left(z,t_1\right), & \beta^{s-2}\mathcal{E}^{*}(z,t_1)\dot{\xi}\left(z,t_2\right), & \cdots, & \mathcal{E}^{*}(z,t_1)\dot{\xi}\left(z,t_s\right)\\
\beta^{s-1}\mathcal{M}^{*}(z)\ddot{\xi}\left(z,t_1\right), & \beta^{s-2}\mathcal{M}(z)\ddot{\xi}\left(z,t_2\right), & \cdots, & \mathcal{M}(z)\ddot{\xi}\left(z,t_s\right)
\end{array}\right]_{s\times 2}^{\top},\\
\boldsymbol{\theta}(z,t_s) &= \left[\begin{array}{c} C_e\left(z,t_s\right)\\ C_m\left(z,t_s\right)\end{array}\right]_{2\times 1},\\
& s\in\mathbb{N}^{+},\quad 1\leqslant s\leqslant m,
\end{aligned}
\tag{4.13}
$$

where $\beta\in(0,1]$ provides different weight on data at different time, and $\beta=1.00$ corresponds to the ordinary least squares algorithm, and $\mathcal{E}^{*}(z,t_s)$ is the time-varying excitation

dimensional item:

$$\mathcal{E}^*(z,t_s)=\frac{\rho D U^2(z)}{2\left|\dot{\xi}_y(z,t_s)\right|}. \tag{4.14}$$

Based on the least square fit algorithm, the parameters to be identified need to minimize the sum of the squared errors between $\boldsymbol{F}_{\boldsymbol{y}}^*(z,t_s)$ and $\boldsymbol{H}_s^*(z,t_s)\boldsymbol{\theta}_s(z,t_s)$ as $J(\boldsymbol{\theta})$, which follows:

$$\left.\frac{\partial J(\boldsymbol{\theta})}{\partial \boldsymbol{\theta}}\right|_{\widehat{\boldsymbol{\theta}}_s}=\left.\frac{\partial}{\partial \boldsymbol{\theta}}\left(\boldsymbol{F}_{\boldsymbol{y}}^*(z,t_s)-\boldsymbol{H}_s^*(z,t_s)\boldsymbol{\theta}_s(z,t_s)\right)^{\top}\left(\boldsymbol{F}_{\boldsymbol{y}}^*-\boldsymbol{H}_s^*(z,t_s)\boldsymbol{\theta}_s(z,t_s)\right)\right|_{\widehat{\boldsymbol{\theta}}_s}=0, \tag{4.15}$$

then we have:

$$\begin{aligned}\widehat{\boldsymbol{\theta}}_s(z,t_s)&=\left(\boldsymbol{H}_s^{*\top}(z,t_s)\boldsymbol{H}_s^*(z,t_s)\right)^{-1}\boldsymbol{H}_s^{*\top}(z,t_s)\boldsymbol{F}_{\boldsymbol{y}}^*(z,t_s)\\&=\left(\boldsymbol{H}_s{}^{\top}(z,t_s)\boldsymbol{L}_s\boldsymbol{H}_s(z,t_s)\right)^{-1}\boldsymbol{H}_s{}^{\top}(z,t_s)\boldsymbol{L}_s\boldsymbol{F}_{\boldsymbol{y}}(z,t_s),\end{aligned} \tag{4.16}$$

where $\boldsymbol{L}_s$ is the weighted matrix, which is a diagonal matrix $\boldsymbol{L}_s=\mathrm{diag}(\mu^{s-1},\mu^{s-2},\ldots,\mu,1)$, $\mu=\beta^2,\mu\in(0,1]$, and μ is called the forgetting factor. The essence of this method is to assign lower weights to the data farther from the current moment of estimation. By traversing the spanwise positions z and the time sequence, the time-domain distributions of the excitation coefficients and added mass coefficients along the riser can be obtained. The time-domain hydrodynamic coefficients exhibit complex temporal variations, as shown in the supplemental material.

Figure 17 shows the instantaneous VIV hydrodynamic coefficients for the linearly sheared flow case $U_m=0.80\,\mathrm{m/s}$ based on simulation results at the $Z/L=0.80$ location. Figure 17(a) shows the IL and CF VIV response in the time domain, subfigure(b) shows the instantaneous excitation coefficient $C_e(t)$ and added mass coefficient $C_m(t)$ based on equation (4.16), and figure 17(c) to (f) show the instantaneous vorticity contours ω_z related to the red dot (left to right) time stamp.

The time-domain characteristics of the added mass coefficient are more complex due to multi-mode and traveling wave phenomena (Huera-Huarte 2025). In previous studies of VIV under uniform flow, negative added mass coefficients are generally associated with P+S or 2P wake patterns (Wang *et al.* 2021*a*). Taking the linearly sheared flow case shown in figure 10(d) as an example, negative values of dominant C_m correspond to a P+S wake shedding pattern. Similarly, under the bidirectional shear flow condition with $U_m=0.99\,\mathrm{m/s}$, as shown in figure 13(d), a 2P wake shedding pattern is also associated with negative dominant C_m values, which was also discovered in previous uniform flow VIV research (Wang *et al.* 2021*a*).

However, at higher flow velocities, the traveling wave behavior of the flexible riser leads to more complex and unsteady wake shedding patterns. The analysis is further extended to investigate this phenomenon by conducting a simplified examination of the time-domain hydrodynamic forces at different sections of the flexible riser under various flow conditions. Figure 18 presents the time-domain vortex-induced hydrodynamic forces at cross-sections of the riser under the bidirectionally sheared flow case of $U_m=0.99\,\mathrm{m/s}$ based on numerical simulation results. In both cases, a pronounced traveling wave response is present. As a result, the VIV response in the time domain is non-stationary and exhibits significant time-varying hydrodynamic characteristics. Examining the wake shedding patterns under the two flow conditions reveals that, for the linearly sheared flow case, the wake shedding transitions from the 2S mode to the P+S mode, as shown in figure 17 (c) to (f), accompanied by a change in the added mass coefficient from positive to negative. It should be noted that wake pattern transitions require time to develop. In figure 17(d), the flow experiences only a very short duration with negative C_m, during which the wake pattern still exhibits a 2S wake pattern. The transition between different wake patterns remains a subject for future investigation.

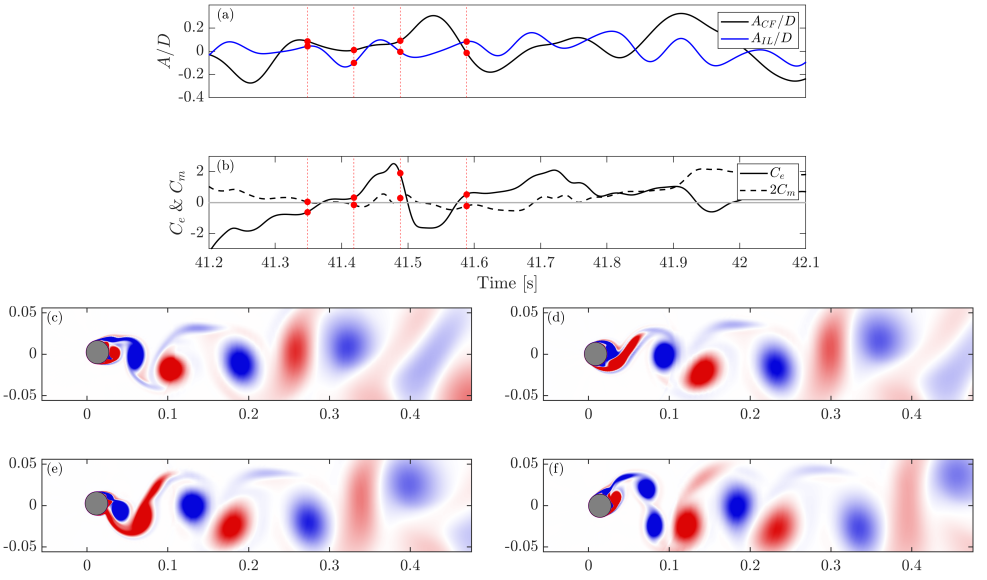

Figure 17: Instantaneous VIV hydrodynamic for linearly sheared flow case $U_m = 0.80\,\mathrm{m/s}$ of simulation at $Z/L = 0.80$ location based on numerical simulation data: (a) VIV response in the CF direction (black line –) and IL direction (blue line –) in time domain. (b) Excitation (black line –) and added mass (black dash line - -) coefficient in the time domain. (c) to (f) Instantaneous vorticity contours ω_z at different time stamps correspond to the red circular dots (•) in subfigures (a) and (b) from left to right (red dash line - -), with $[-35, 35]$ range. Subfigures (c), (d) and (e): 2S wake pattern; Subfigure (f): P+S wake pattern. Negative C_m: subfigures (b) and (f).

For the bidirectionally sheared flow case, the added-mass coefficient exhibits a clear time-domain transition from positive to negative. Correspondingly, the wake shedding evolves across four instantaneous vorticity contours through a sequence of 2S (figure 18(c)) → P+S (figure 18(e)) → 2P patterns (figure 18(f)). Therefore, for both linearly sheared and bidirectionally sheared flows, negative instantaneous C_m is consistently associated with the emergence of pronounced P+S and 2P wake patterns, in agreement with observations for uniform flow VIV (Fan *et al.* 2019*b*). In this context, our results indicate that, for the final question posed in §1, the added mass coefficient in bidirectionally sheared flow VIV remains closely linked to the P+S and 2P wake regimes, consistent with prior uniform flow VIV studies.

5. Conclusions and future work

This study investigates the hydrodynamic characteristics of a flexible pipe undergoing vortex-induced vibration in bidirectionally sheared flow, inspired by subsurface currents induced by internal solitons, which occur widely in the ocean. Through a combination of experimental measurements and validated numerical simulations, the effects of antisymmetric background flow on the structural response and hydrodynamic properties are systematically explored. The Reynolds number in the present study ranges from 8523 to 39 490, which lies within the subcritical regime (Achenbach 1971). This range covers most Reynolds numbers commonly investigated in VIV studies (Trim *et al.* 2005; Vandiver *et al.* 2005; Fan *et al.* 2019*b*). However, extending the analysis to higher Reynolds numbers is necessary to more systematically characterize VIV response under bidirectionally sheared flow.

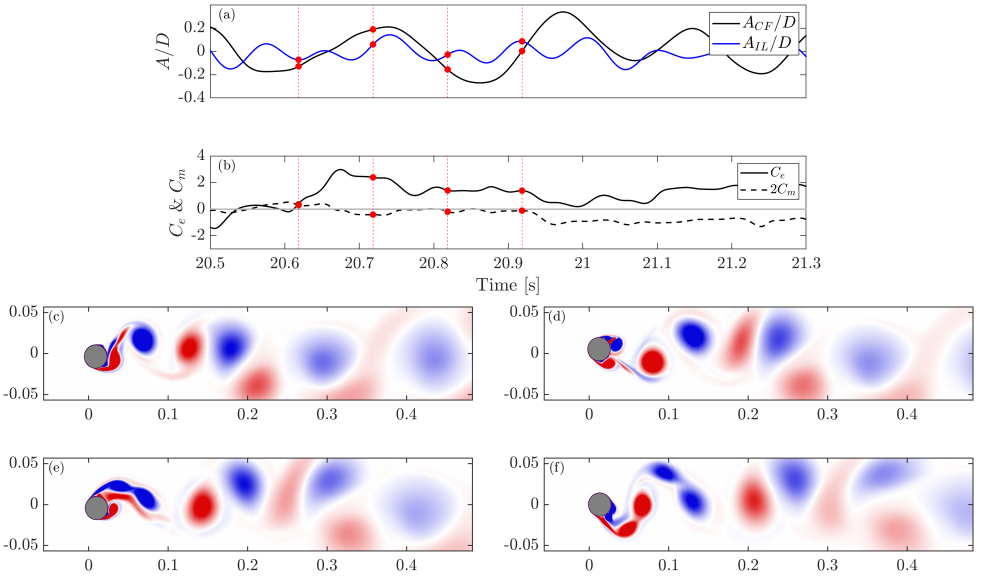

Figure 18: Instantaneous VIV hydrodynamic for bidirectionally sheared flow case U_m = 0.99 m/s of simulation at $Z/L = 0.90$ location based on numerical simulation data: (a) VIV response in the CF direction (black line –) and IL direction (blue line –) in time domain. (b) Excitation (black line –), added mass (black dash line - -) coefficient in the time domain, and the gray line – represents the zero value. (c) to (f) Instantaneous vorticity contours ω_z at different time stamps correspond to the red circular dots (•) in subfigures (a) and (b) from left to right (red dash line - -), with $[-35, 35]$ range. Subfigures (c) and (d): 2S wake pattern; Subfigure (e): P+S wake pattern; subfigure (f): 2P wake pattern. Positive C_m: subfigure (c); negative C_m: subfigures (d) to (f).

The mean in-line displacement exhibits a nearly antisymmetric distribution, and a quadratic relation is observed between the maximum displacement and flow velocity. The mean drag coefficient remains nearly constant across different Reynolds numbers with an average value of $\overline{C_{dm}} = 1.47$, showing that the mean drag coefficient only has a weak dependence on the flow velocity of bidirectionally sheared flows. The resulting shear force and bending moment distributions differ from those in uniform flow VIV, exhibiting a maximum shear force near the mid-span and an antisymmetric bending moment profile resembling a sinusoidal function along the spanwise direction. Corresponding empirical formulas for the peak shear force and maximum moment are proposed. The relationship between spanwise distributions of VIV response and drag coefficients remains unclear and will be a topic for further investigation.

The dominant frequency hydrodynamic analysis shows that the coefficient C_e distribution is approximately symmetric about the mid-span, whereas the added mass coefficient C_m remains close to unity over most of the length. The phase difference between the cross-flow and in-line responses retains an antisymmetric pattern, with phase jumps of nearly π at the nodes of in-line modal shapes. In the time domain, significant unsteadiness in the hydrodynamic coefficients is captured using the forgetting-factor least squares approach. Notably, negative instantaneous added mass coefficients are observed during transitions to P+S and 2P wake patterns, indicating a strong correlation between unsteady wake dynamics and added mass variation. However, the relationship between added-mass oscillations and wake-pattern transitions remains unclear, and further research for higher *Re* is needed to

examine transition intermittency and hysteresis, using either scaled experiments with particle image velocimetry (Raffel *et al.* 2018) or complementary CFD studies.

Spectral proper orthogonal decomposition (SPOD) of the flow field provides further insights into flow-structure interaction. At lower flow velocities, the dominant frequency distribution closely follows the background velocity profile, indicating that the fluid dynamics are governed by the Strouhal law. At higher velocities, the dominant frequencies become symmetric and align with the structural vibration dominant frequency distribution, suggesting SPOD as a new analysis tool for the lock-in phenomenon in flexible pipe VIV.

The present study opens several directions for future research. The simulation framework can be extended to more complex pipe systems, such as pipe clusters and configurations with geometric complexity and time-varying flow conditions. In addition, SPOD offers a potential tool for analyzing VIV such as connections between the hydrodynamic coefficient and the SPOD result, and mechanism analysis of the flexible pipe lock-in phenomenon (Bourguet *et al.* 2013). Fu *et al.* (2025*b*) provided a comprehensive steady flow experimental benchmark dataset for validating the simulation code, and the corresponding hydrodynamic analysis is presented in the current work. However, there also contain additional VIV experimental phenomena that cannot be fully explained by the experimental results alone, representing a key objective for future simulation efforts. This will also facilitate future work aimed at analyzing the shear rate of the flow profile, as systematically investigating the underlying VIV mechanisms across this parameter space through experiment will be conducted in the future.

Acknowledgment

X.F., S.F., J.S., Z.N. gratefully acknowledge the National Science Fund for Distinguished Young Scholars (Grant No. 52425102), and the continuous support from FIFERS JIP. C.L. receives no support in this work.

Declaration of interests

The authors report no conflicts of interest.

Data availability

The data that support the findings of this study are openly available in GitHub repository: https://github.com/xuepengfu/VIVdatashare.

Appendix A. Experimental apparatus credibility analysis

In this appendix, we summarize the credibility analysis of the experimental apparatus based on our published work (Fu *et al.* 2022*a*), covering five aspects: (1) the influence of the wake generated by the upstream cylinder; (2) the time history of the VIV response; (3) water-depth effects; (4) noise induced by the experimental apparatus; and (5) experimental repeatability.

(1) To obtain sufficient strain measurements for VIV analysis, the test pipe completes one full revolution in each run. Because the flow encountered during the second half-revolution is influenced by turbulence generated during the first half-revolution, we evaluate and discuss the effect on the measured VIV strain response. Figure 19 compares the CF strain measurements obtained from one full revolution of the test pipe and from the two half-revolutions separately for a representative case $U_m = 0.48\,\mathrm{m/s}$. As shown in figure 19(a), the spanwise distributions of the RMS strain ε_{rms} from the three datasets nearly collapse

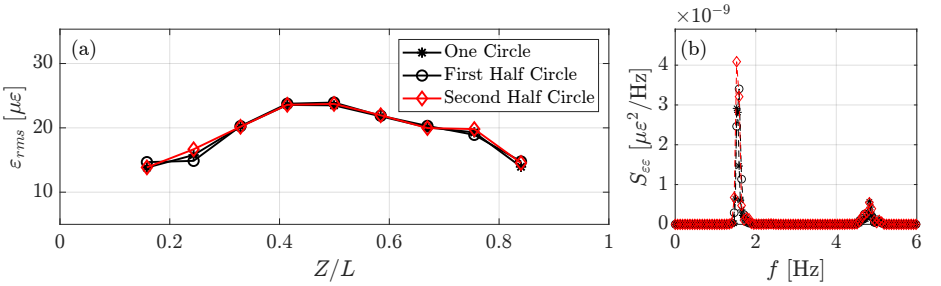

Figure 19: Comparison of CF strain data based on the one circle, the first half-circle and the second half-circle in case $U_m = 0.48\,\mathrm{m/s}$ ($Re_m = 1.37 \times 10^4$). (a) root-mean-square of CF strains at measuring points along the test pipe. (b) Power spectral densities of CF strains at the fifth sensor point of $Z/L = 0.50$. In figure labels, $\mu\varepsilon$ denotes the microstrain measurement.

over the entire length, with only minor deviations at a few sensor locations, indicating that the overall strain amplitude is insensitive to whether the data are taken from the first half-circle, the second half-circle, or the full circle. Consistently, figure 19(b) shows that the strain power spectral densities at $Z/L = 0.50$ exhibit the same dominant frequency peak for all three datasets, while the secondary peaks and broadband levels remain very close. Overall, these comparisons suggest that potential wake effects from the first half-revolution have a negligible influence on the dominant VIV response, and the difference in the overall strain RMS level is 2.7% with limited effect.

(2) The VIV time histories were also examined to ensure that a sufficiently long interval of statistically steady response was recorded for subsequent analysis. The results indicate that the time histories of our measurements contain nearly 50 VIV response periods, which is at the same level as the different experiment (Trim *et al.* 2005) and sufficient for analysis.

(3) To minimize free-surface effects, four water depths, 1.00 m, 1.20 m, 1.30 m, and 1.40 m, were tested to identify an appropriate experimental depth. The apparatus height is 0.73 m (Fu *et al.* 2022*a*), and the corresponding distances between the pipe and the free surface are approximately $9.20D$, $16.20D$, $19.80D$, and $23.30D$, respectively. The overall differences of VIV strain among the four water-depth cases are within 7%. Therefore, the most conservative depth 1.40 m was selected for the formal experiments.

(4) As shown in figure 2, the experimental apparatus comprises a complex mechanical system. During operation, these components inevitably generate mechanical noise. We assess the magnitude of this noise by comparing results from air tests and underwater tests. Figure 20 compares the measured strain time histories at $Z/L = 0.50$ for case $U_m = 1.39\,\mathrm{m/s}$ when the pipe is tested in water and when it is operated in air. The strain signal in air remains close to the zero baseline and is at least two orders of magnitude smaller than the VIV-induced strain in water, indicating that the mechanical/electrical background noise is less than 1% of the VIV signal amplitude. Therefore, the influence of the experimental apparatus on the measured VIV strain response is negligible for the present tests.

(5) One repeat test at $U_m = 0.99\,\mathrm{m/s}$ was conducted to strengthen the credibility of the VIV measurements. For the repeated run, the relative differences in CF displacement among all measurement points remain below 5%, and the maximum RMS VIV displacement is nearly identical, which demonstrates good experimental repeatability.

In summary, the above checks indicate that the present experimental facility provides reliable and repeatable measurements for the subsequent VIV hydrodynamic analyses. It should be noted that this appendix only provides a concise credibility summary for completeness, and the more comprehensive assessment of the apparatus and measurement methodology

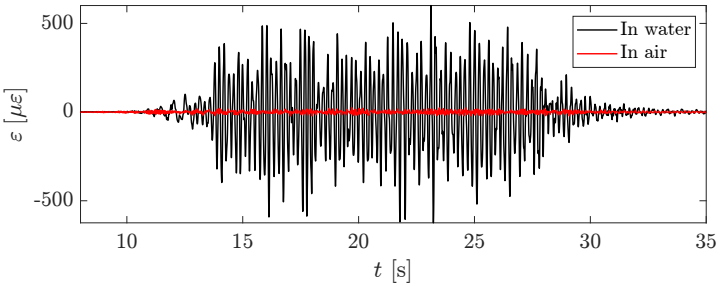

Figure 20: Time histories of the measured strain at $Z/L = 0.50$ for case $U_m = 1.39\,\mathrm{m/s}$. The black curve shows the strain recorded in water (VIV response), whereas the red curve shows the strain recorded in air (background mechanical noise). Here, $\mu\varepsilon$ indicates the microstrain measurement.

can be found in our previous work in Fu *et al.* (2022*a*). In addition to the bidirectionally sheared flow experiments, the updated experimental apparatus has also been used to conduct oscillatory sheared flow VIV experiments, as reported by Fu *et al.* (2024).

Appendix B. Modal analysis in VIV experiment

The displacement response in the IL and CF directions is reconstructed using a modal analysis method based on the measured strain data. Figure 21 shows the detailed layout of the CF and IL FBG strain sensors. In total, nine and fourteen sensors are installed to measure strains in the CF and IL directions, respectively. As illustrated in the unfold view, the sensors are distributed along the pipe spanwise coordinate and grouped into four longitudinal arrays as CF1/CF2 and IL1/IL2. The cross-section view shows that the two arrays for each direction are placed at opposite circumferential locations (separated by 180°), with the CF and IL pairs oriented 90° apart, enabling independent reconstruction of VIV response in two directions.

Assuming small deformation, the displacement in the CF direction $\xi_y(z,t)$ can be expressed as a linear combination of mode shapes:

$$\xi_y(z,t) = \sum_{i=1}^{n} q_i(t)\phi_i(z), \quad z \in [0, L], \tag{B 1}$$

where $q_i(t)$ is the time-dependent modal weight, and $\phi_i(z)$ is the ith spatial mode shape.

The corresponding bending strain $\varepsilon_y(z,t)$ is related to the curvature and pipe radius $R = D/2$ shown in table 1:

$$\varepsilon_y(z,t) = R\frac{\partial^2 \xi_y}{\partial z^2} = R\sum_{i=1}^{n} q_i(t)\phi_i''(z). \tag{B 2}$$

For the beam structure with pin-pin end, the ith mode shape is as follows:

$$\phi_i(z) = \sin\left(\frac{i\pi z}{L}\right), \quad i = 1, 2, \cdots \tag{B 3}$$

with the corresponding curvature:

$$\phi_i''(z) = -\left(\frac{i\pi}{L}\right)^2 \phi_i(z). \tag{B 4}$$

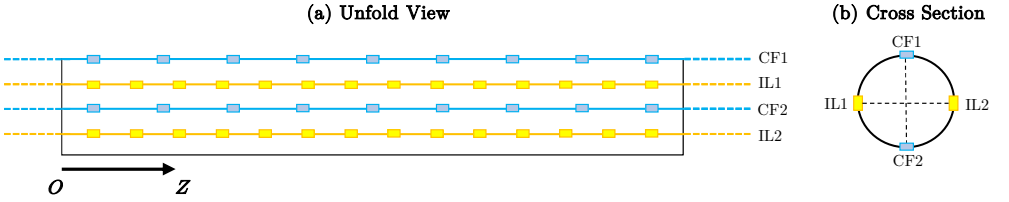

Figure 21: Distribution of FBG strain sensors along test pipe model. Blue blocks denote the strain sensors in the CF direction, and yellow blocks denote the strain sensors in the IL direction. (a) Unfold view. (b) Cross-section view.

Thus, the strain becomes

$$\varepsilon_y(z,t) = -R\sum_{i=1}^{n}\left(\frac{i\pi}{L}\right)^2 q_i(t)\phi_i(z). \tag{B 5}$$

Given the measured strain $\varepsilon_y(z,t)$ and known $\phi_i(z)$, the modal weights $q_i(t)$ can be identified via projection or regression. The displacement is then reconstructed using equation (B 1). To eliminate high-mode noise, modes are selected based on a curvature RMS threshold: modes with RMS values above 10% of the maximum are retained (Lie & Kaasen 2006).

This modal reconstruction approach enables time-resolved displacement estimation from distributed strain measurements in both IL and CF directions. This approach has shown great accuracy for establishing the VIV displacement, and more details for this method are provided Fu *et al.* (2022*a*), Huera-Huarte (2006), and Lie & Kaasen (2006).

REFERENCES

Achenbach, E. 1971 Influence of surface roughness on the cross-flow around a circular cylinder. *J. Fluid Mech.* **46** (2), 321–335.

Aronsen, K. H. & Larsen, C. M. 2007 Hydrodynamic coefficients for in-line vortex induced vibrations. *International Conference on Offshore Mechanics and Arctic Engineering*, vol. Volume 3: Pipeline and Riser Technology; CFD and VIV, pp. 949–956.

Baarholm, G. S., Larsen, C. M. & Lie, H. 2006 On fatigue damage accumulation from in-line and cross-flow vortex-induced vibrations on risers. *J. Fluids Struct.* **22** (1), 109–127.

Bao, Y., Palacios, R., Graham, M. & Sherwin, S. 2016 Generalized thick strip modelling for vortex-induced vibration of long flexible cylinders. *J. Comput. Phys.* **321**, 1079–1097.

Bearman, P. W. 1984 Vortex shedding from oscillating bluff bodies. *Annu. Rev. Fluid Mech.* **16**, 195–222.

Benner, B. M., Carleton, A. G. & Modarres-Sadeghi, Y. 2025 Transition from vortex-induced vibrations to galloping in a flexible square prism. *J. Fluid Mech.* **1007**, A76.

Bourguet, R., Karniadakis, G. E. & Triantafyllou, M. S. 2011*a* Vortex-induced vibrations of a long flexible cylinder in shear flow. *J. Fluid Mech.* **677**, 342–382.

Bourguet, R., Karniadakis, G. E. & Triantafyllou, M. S. 2013 Distributed lock-in drives broadband vortex-induced vibrations of a long flexible cylinder in shear flow. *J. Fluid Mech.* **717**, 361–375.

Bourguet, R., Lucor, D. & Triantafyllou, M. S. 2012 Mono- and multi-frequency vortex-induced vibrations of a long tensioned beam in shear flow. *J. Fluids Struct.* **32**, 52–64.

Bourguet, R., Modarres-Sadeghi, Y., Karniadakis, G. E. & Triantafyllou, M. S. 2011*b* Wake-body resonance of long flexible structures is dominated by counterclockwise orbits. *Phys. Rev. Lett.* **107** (13), 134502.

Chaplin, J. R., Bearman, P.W., Huera-Huarte, F. J. & Pattenden, R. J. 2005 Laboratory measurements of vortex-induced vibrations of a vertical tension riser in a stepped current. *J. Fluids Struct.* **21** (1), 3–24.

Cheng, Z., Zhang, J. H., Wang, R., Lien, F. & Dowell, E. H. 2024 Asymmetric instability of flow-induced vibration for elastically mounted cube at moderate Reynolds numbers. *J. Fluid Mech.* **996**, A34.

Clough, R. W. & Penzien, J. 2003 *Dynamics of Structures*, 3rd edn. Berkeley, California, USA: Computers & Structures, Inc.

Dahl, J. M. 2008 Vortex-induced vibration of a circular cylinder with combined in-line and cross-flow motion. PhD thesis, Massachusetts Institute of Technology, Cambridge.

Dahl, J. M., Hover, F. S., Triantafyllou, M. S., Dong, S. & Karniadakis, G. E. 2007 Resonant vibrations of bluff bodies cause multivortex shedding and high frequency forces. *Phys. Rev. Lett.* **99** (14), 144503.

Dahl, J. M., Hover, F. S., Triantafyllou, M. S. & Oakley, O. H. 2010 Dual resonance in vortex-induced vibrations at subcritical and supercritical Reynolds numbers. *J. Fluid Mech.* **643**, 395–424.

Deng, D., Zhao, W. & Wan, D. 2020 Vortex-induced vibration prediction of a flexible cylinder by three-dimensional strip model. *Ocean Eng.* **205**, 107318.

Duan, J., Zhou, J., You, Y. & Wang, X. 2021 Effect of internal flow on vortex-induced vibration dynamics of a flexible mining riser in external shear current. *Mar. Struct.* **80**, 103094.

Evangelinos, C. & Karniadakis, G. E. 1999 Dynamics and flow structures in the turbulent wake of rigid and flexible cylinders subject to vortex-induced vibrations. *J. Fluid Mech.* **400**, 91–124.

Fan, D., Jodin, G., Consi, T. R., Bonfiglio, L., Ma, Y., Keyes, L. R., Karniadakis, G. E. & Triantafyllou, M. S. 2019*a* A robotic intelligent towing tank for learning complex fluid-structure dynamics. *Sci. Robot.* **4** (36), eaay5063.

Fan, D., Wang, Z., Triantafyllou, M. S. & Karniadakis, G. E. 2019*b* Mapping the properties of the vortex-induced vibrations of flexible cylinders in uniform oncoming flow. *J. Fluid Mech.* **881**, 815–858.

Fortescue, T. R., Kershenbaum, L. S. & Ydstie, B. E. 1981 Implementation of self-tuning regulators with variable forgetting factors. *Autom.* **17** (6), 831–835.

Fu, X., Fu, S., Han, Z., Niu, Z., Zhang, M. & Zhao, B. 2025*a* Numerical simulations of 2-DOF vortex-induced vibration of a circular cylinder in two and three dimensions: A comparison study. *J. Ocean Eng. Sci.* **10** (4), 395–410.

Fu, X., Fu, S., Niu, Z., Zhao, B., Shen, J. & Deng, P. 2025*b* A validated fluid–structure interaction simulation model for vortex-induced vibration of a flexible pipe in steady flow. *Mar. Struct.* **104**, 103895.

Fu, X., Fu, S., Ren, H., Xie, W., Xu, Yu., Zhang, M., Liu, Z. & Meng, S. 2022*a* Experimental investigation of vortex-induced vibration of a flexible pipe in bidirectionally sheared flow. *J. Fluids Struct.* **114**, 103722.

Fu, X., Fu, S., Zhang, M., Han, Z., Ren, H., Xu, Yu. & Zhao, B. 2022*b* Frequency capture phenomenon in tandem cylinders with different diameters undergoing flow-induced vibration. *Phys. Fluids* **34** (8), 085120.

Fu, X., Fu, S., Zhang, M., Ren, H., Zhao, B. & Xu, Y. 2024 Vortex-induced vibration of a flexible pipe under oscillatory sheared flow. *Phys. Rev. Fluids* **9** (1), 014604.

Fu, X., Vijayakumar, G., Lee, B. & Sprague, M. 2026 Numerical simulation of vortex-induced vibration response of a single IEA 10-MW wind turbine blade. *J. Fluids Struct.* **143**, 104537.

Fu, X., Zhang, M., Fu, S., Zhao, B., Ren, H. & Xu, Y. 2022*c* On the study of vortex-induced vibration of a straked pipe in bidirectionally sheared flow. *Ocean Eng.* **266**, 112945.

Gabbai, R. D. & Benaroya, H. 2005 An overview of modeling and experiments of vortex-induced vibration of circular cylinders. *J. Sound Vib.* **282** (3-5), 575–616.

Garrett, C. & Munk, W. 1979 Internal waves in the ocean. *Annu. Rev. Fluid Mech.* **11** (1), 339–369.

Ge, Y., Zhao, L. & Cao, J. 2022 Case study of vortex-induced vibration and mitigation mechanism for a long-span suspension bridge. *J. Wind Eng. Ind. Aerodyn.* **220**, 104866.

Gopalkrishnan, R. 1993 Vortex-induced forces on oscillating bluff cylinders. PhD thesis, Massachusetts Institute of Technology.

Govardhan, R. & Williamson, C. H. K. 2000 Modes of vortex formation and frequency response of a freely vibrating cylinder. *J. Fluid Mech.* **420**, 85–130.

Govardhan, R. & Williamson, C. H. K. 2006 Defining the 'modified griffin plot' in vortex-induced vibration: revealing the effect of Reynolds number using controlled damping. *J. Fluid. Mech.* **561**, 147–180.

Grindergslev, C., Nørmark Sørensen, N., Raimund Pirrung, G. & González Horcas, S. 2022 Multiple limit cycle amplitudes in high-fidelity predictions of standstill wind turbine blade vibrations. *Wind Energy Sci.* **7** (6), 2201–2213.

Han, P., De Langre, E., Thompson, M. C., Hourigan, K. & Zhao, J. 2023 Vortex-induced vibration forever even with high structural damping. *J. Fluid Mech.* **962**, A13.

Huera-Huarte, F. J. 2006 Multi-mode vortex-induced vibrations of a flexible circular cylinder. PhD thesis, University of London.

Huera-Huarte, F. J. 2025 Vortex-induced vibration of flexible cylinders in cross-flow. *Annu. Rev. Fluid Mech.* **57**, 285–310.

Huera-Huarte, F. J., Bearman, P. W. & Chaplin, J. R. 2006 On the force distribution along the axis of a flexible circular cylinder undergoing multi-mode vortex-induced vibrations. *J. Fluids Struct.* **22** (6-7), 897–903.

Jacobs, S. S., Jenkins, A., Giulivi, C. F. & Dutrieux, P. 2011 Stronger ocean circulation and increased melting under pine island glacier ice shelf. *Nat. Geosci.* **4** (8), 519–523.

Jasak, H. 1996 Error analysis and estimation in the finite volume method with applications to fluid flows. PhD thesis, Imperial College London, London.

Jhingran, V., Jaiswal, J. & Vandiver, J. K. 2008 Spatial variation of drag on long cylinders in sheared flow. *International Conference on Offshore Mechanics and Arctic Engineering*, vol. Volume 5: Materials Technology; CFD and VIV, pp. 919–927.

Jung, S. Y., Kim, J. J., Park, H. W. & Lee, S. J. 2018 Comparison of flow structures behind rigid and flexible finite cylinders. *Int. J. Mech. Sci.* **142**, 480–490.

Khalak, A. & Williamson, C. H. K. 1997 Investigation of relative effects of mass and damping in vortex-induced vibration of a circular cylinder. *J. Wind Eng. Ind. Aerodyn.* **69**, 341–350.

Kim, S. W., Sævik, S., Wu, J. & Leira, B. J. 2022 Time domain simulation of marine riser vortex-induced vibrations in three-dimensional currents. *Appl. Ocean Res.* **120**, 103057.

Lie, H. & Kaasen, K. E. 2006 Modal analysis of measurements from a large-scale VIV model test of a riser in linearly sheared flow. *J. Fluids Struct.* **22** (4), 557–575.

Lilly, J. M. & Olhede, S. C. 2012 Generalized morse wavelets as a superfamily of analytic wavelets. *IEEE Trans. Signal Process.* **60** (11), 6036–6041.

Liu, C., Fu, S., Zhang, M. & Ren, H. 2018 Time-varying hydrodynamics of a flexible riser under multi-frequency vortex-induced vibrations. *J. Fluids Struct.* **80**, 217–244.

Liu, C., Fu, S., Zhang, M., Ren, H. & Xu, Y. 2020 Hydrodynamics of a flexible cylinder under modulated vortex-induced vibrations. *J. Fluids Struct.* **94**, 102913.

Livanos, D. 2018 Investigation of vortex induced vibrations on wind turbine towers. Master's thesis, Delft University of Technology.

Ma, L., Lin, K., Fan, D., Wang, J. & Triantafyllou, M. S. 2022 Flexible cylinder flow-induced vibration. *Phys. Fluids* **34** (1), 011302.

MacKinnon, J. A. et al. 2017 Climate process team on internal wave–driven ocean mixing. *Bull. Am. Meteorol. Soc.* **98** (11), 2429–2454.

Maleki, A., Grace, S., Mankbadi, R. R. & Golubev, V. V. 2026 Influence of inflow turbulence on wake dynamics of a square cylinder. *J. Fluid Mech.* **1028**, A15.

Minowa, M., Sugiyama, S., Ito, M., Yamane, S. & Aoki, S. 2021 Thermohaline structure and circulation beneath the Langhovde Glacier ice shelf in East Antarctica. *Nat. Commun.* **12** (1), 4209.

Modarres-Sadeghi, Y., Mukundan, H., Dahl, J. M., Hover, F. S. & Triantafyllou, M. S. 2010 The effect of higher harmonic forces on fatigue life of marine risers. *J. Sound Vib.* **329** (1), 43–55.

Newman, D. J. & Karniadakis, G. E. 1997 A direct numerical simulation study of flow past a freely vibrating cable. *J. Fluid Mech.* **344**, 95–136.

Nielsen, F. G., Søreide, T. H. & Kvarme, S. O. 2002 VIV response of long free spanning pipelines. *International Conference on Offshore Mechanics and Arctic Engineering*, vol. 36118, pp. 121–129.

O'Neill, C. M., Schubert, Y., Sieber, M., Martinuzzi, R. & Morton, C. 2021 Application of SPOD analysis to PIV data obtained in the wake of a circular cylinder undergoing vortex induced vibrations. *14th International Symposium on Particle Image Velocimetry* **1** (1).

Patel, U. N., Rothstein, J. P. & Modarres-Sadeghi, Y. 2023 Forced oscillations of a cylinder in the flow of viscoelastic fluids. *J. Fluid Mech.* **975**, A28.

Raffel, M., Willert, C. E., Scarano, F., Kähler, C. J., Wereley, S. T. & Kompenhans, J. 2018 *Particle Image Velocimetry*, 3rd edn. Cham: Springer.

Resvanis, T. L & Vandiver, J. K. 2022 Efficient measurement of hydrodynamic coefficients for vibrating cylinders at supercritical Reynolds numbers. *J. Fluids Struct.* **108**, 103427.

Sarpkaya, T. 1995 Hydrodynamic damping, flow-induced oscillations, and biharmonic response. *J. Offshore Mech. Arct. Eng.* **117** (4), 232–238.

Sarpkaya, Turgut 2004 A critical review of the intrinsic nature of vortex-induced vibrations. *J. Fluids Struct.* **19** (4), 389–447.

Schmidt, O. T. & Colonius, T. 2020 Guide to spectral proper orthogonal decomposition. *AIAA J.* **58** (3), 1023–1033.

Sieber, M., Paschereit, C. O. & Oberleithner, K. 2016 Spectral proper orthogonal decomposition. *J. Fluid Mech.* **792**, 798–828.

Song, L., Fu, S., Cao, J., Ma, L. & Wu, J. 2016*a* An investigation into the hydrodynamics of a flexible riser undergoing vortex-induced vibration. *J. Fluids Struct.* **63**, 325–350.

Song, L., Fu, S., Dai, S., Zhang, M. & Chen, Y. 2016*b* Distribution of drag force coefficient along a flexible riser undergoing VIV in sheared flow. *Ocean. Eng.* **126**, 1–11.

Thorsen, M. J., Sævik, S. & Larsen, C. M. 2017 Non-linear time domain analysis of cross-flow vortex-induced vibrations. *Mar. Struct.* **51**, 134–151.

Tian, C., Zhu, J., Holmedal, L. E., Andersson, H. I., Jiang, F. & Pettersen, B. 2023 How vortex dynamics affects the structural load in step cylinder flow. *J. Fluid Mech.* **972**, A10.

Tognarelli, M. A., Slocum, S. T., Frank, W. R. & Campbell, R. B. 2004 VIV response of a long flexible cylinder in uniform and linearly sheared currents. In *Offshore Technology Conference*, pp. OTC–16338.

Towne, A., Schmidt, O. T. & Colonius, T. 2018 Spectral proper orthogonal decomposition and its relationship to dynamic mode decomposition and resolvent analysis. *J. Fluid Mech.* **847**, 821–867.

Trim, A. D., Braaten, H., Lie, H. & Tognarelli, M. A. 2005 Experimental investigation of vortex-induced vibration of long marine risers. *J. Fluids Struct.* **21** (3), 335–361.

Vandiver, J. K. 1983 Drag coefficients of long flexible cylinders. In *OTC Offshore Technology Conference*, pp. OTC–4490–MS.

Vandiver, J. K., Marcollo, H., Swithenbank, S. & Jhingran, V. 2005 High mode number vortex-induced vibration field experiments. In *Offshore Technology Conference*, pp. OTC–17383. OTC.

Wang, Z., Fan, D. & Triantafyllou, M. S. 2021*a* Illuminating the complex role of the added mass during vortex induced vibration. *Phys. Fluids* **33** (8), 085120.

Wang, Z., Fan, D., Triantafyllou, M. S. & Karniadakis, G. E. 2021*b* A large-eddy simulation study on the similarity between free vibrations of a flexible cylinder and forced vibrations of a rigid cylinder. *J. Fluids Struct.* **101**, 103223.

Willden, R. H. J. & Graham, J. M. R. 2001 Numerical prediction of VIV on long flexible circular cylinders. *J. Fluids Struct.* **15** (3-4), 659–669.

Willden, R. H. J. & Graham, J. M. R. 2004 Multi-modal vortex-induced vibrations of a vertical riser pipe subject to a uniform current profile. *Eur. J. Mech. B Fluids* **23** (1), 209–218.

Willert, C. 2025 Event-based particle image velocimetry for high-speed flows. *Meas. Sci. Technol.* **36** (7), 075302.

Williamson, C. H. K. & Govardhan, R. 2004 Vortex-induced vibrations. *Annu. Rev. Fluid Mech.* **36** (1), 413–455.

Williamson, C. H. K. & Govardhan, R. 2008 A brief review of recent results in vortex-induced vibrations. *J. Wind Eng. Ind. Aerodyn.* **96** (6-7), 713–735.

Wu, J. 2011 Hydrodynamic force identification from stochastic vortex induced vibration experiments with slender beams. PhD thesis, Norwegian University of Science and Technology.

Wu, J., Jiang, F., Lie, H.r, Passano, E., Yin, D., Sævik, S., Grytøyr, G., Hogg, B. F., Resvanis, T. & Vandiver, J. K. 2023 Evaluation of VIV prediction practice of deep-water steel lazy wave risers (SLWRs). *International Conference on Offshore Mechanics and Arctic Engineering*, vol. Volume 7: CFD & FSI, p. V007T08A033.

Xie, B., Li, J., Ren, X. & Lei, F. 2018 The characteristic analysis of internal solitons in the Liuhua area of the South China Sea. In *ISOPE International Ocean and Polar Engineering Conference*, p. ISOPE. ISOPE.

Yin, D. & Larsen, C. M. 2011 Experimental and numerical analysis of forced motion of a circular cylinder. *International Conference on Offshore Mechanics and Arctic Engineering*, vol. Volume 7: CFD and VIV; Offshore Geotechnics, pp. 327–336.

Zheng, H., Dahl, J. M., Modarres-Sadeghi, Y. & Triantafyllou, M. S. 2014*a* Coupled inline-cross flow VIV hydrodynamic coefficients database. *International Conference on Offshore Mechanics and Arctic Engineering*, vol. Volume 2: CFD and VIV, p. V002T08A087.

Zheng, H., Price, R. E., Modarres-Sadeghi, Y. & Triantafyllou, M. S. 2014*b* On fatigue damage of long flexible cylinders due to the higher harmonic force components and chaotic vortex-induced vibrations. *Ocean Eng.* **88**, 318–329.

Zhou, H. & Zheng, C. 2023 Comparing SPOD and POD for wake flow of tandem oscillating cylinders. In *AIAA AVIATION 2023 Forum*, p. 4255.